TOWARD THE DESIGN AND CHARACTERIZATION OF A DYNAMICALLY SIMILAR ARTIFICIAL INSECT WING

by

Heidi Elita Reid

A thesis submitted in partial fulfillment
of the requirements for the degree

of

Master of Science

in

Mechanical Engineering

MONTANA STATE UNIVERSITY
Bozeman, Montana

November 2019

©COPYRIGHT

by

Heidi Elita Reid

2019

All Rights Reserved

ACKNOWLEDGEMENTS

I want to thank my collaborators in the Montana State University entomology laboratory, Dr. Robert Peterson and Miles Maxcer, for rearing our hawkmoths; and my collaborators at Binghamton State University of New York, Dr. Jia Deng and Huimin Zhou, for manufacturing our wings and working with us on design iterations. I would also like to thank my colleagues in Montana State University's Bio-inspired Dynamics Laboratory for supporting my research. I'd also like to thank my master's committee, Dr. Mark Jankauski, Dr. Erick Johnson, and Dr. Cecily Ryan for all their support throughout my research process. And finally, I would like to acknowledge that my research was supported in part by NSF Grant CBET-1855383. Thank you, all.

TABLE OF CONTENTS

1. INTRODUCTION 1

Background 3
Objectives and Novelty 9

2. PARAMETRIC STUDIES TO GUIDE WING DESIGN 13

Preliminary Base Excitation Tests with a Flat Rectangular Shim 14
Rectangular Model with Varying Linear and Bilinear Thickness Distribution 18
Linear Thickness Variation 18
Bilinear Thickness Variation 22
Effects of Camber on a Rectangular Shim 23
Determination of Mass Distribution 25
Parametric Studies Summary 27

3. DYNAMIC TESTING OF BIOLOGICAL AND ARTIFICIAL WINGS 28

Dynamic Wing Experimental Setup 28
Insect Preparation 29
Dynamic Characterization of Biological and Artificial Insect Wings 30
Dynamic Biological Wing Data 35
Artificial Wing Manufacture 37
Comparison of Biological to Artificial Wing Response 40
Results and Discussion on the Second Mode 43

4. FEA MODELING 47

Artificial Wing Finite Element Model 47
Flat Wing Model 49
Cambered Wing Model 50

5. CONCLUSION 53

REFERENCES CITED 56

APPENDICES 61

APPENDIX A: MATLAB Codes 62
APPENDIX B: Directionally 3D Printed Beam Modal Analysis 69
APPENDIX C: Biological Wing Mass Distribution Cut Pattern 72

LIST OF TABLES

Table Page

1. Table 3.1: My dynamic biological wing data compared to Literature values 36

2. Table 3.2: Statistical data on first and second modes for biological And artificial wings in air.....41

3. Table B.2: First natural frequencies of directionally 3D Printed beams 71

LIST OF FIGURES

Figure Page

1. Figure 1.1: DelFly 2

2. Figure 1.2: *Manduca sexta* hawkmoth 4

3. Figure 1.3: Vibration spectrum/Frequency Response Function 10

4. Figure 1.4: Mode shapes of a rectangular shim 10

5. Figure 2.1: Experimental setup 16

6. Figure 2.2: First two modes compared in FEA and vibrometer scans 17

7. Figure 2.3: Spanwise and chordwise linear thickness tapered models 18

8. Figure 2.4: Plot of spanwise and chordwise thickness distribution relationship to changes in natural frequency 20

9. Figure 2.4: Plot of bilinear thickness gradation on a rectangular shim 23

10. Figure 2.5: Cambered FEA model compared to camber in an actual hawkmoth wing 24

11. Figure 2.6: Plot of camber variation versus natural frequency 25

12. Figure 2.7: Thickness variation in a hawkmoth wing 27

13. Figure 3.1: Experimental clamping mechanism to preserve camber 30

14. Figure 3.2: Artificial wing design iterations 38

15. Figure 3.3: Exploded CAD model of artificial wing design 39

16. Figure 3.4: Plot of first mode for artificial and biological wings 42

17. Figure 3.5: First bending modes of an artificial wing and a biological wing 43

18. Figure 4.1: Mode shapes of a flat artificial wing in FEA and rendered by the vibrometer 50

LIST OF FIGURES CONTINUED

19. Figure 4.2: Mode shapes of cambered FEA model compared to actual artificial cambered wing 52

20. Figure C.1: Biological wing mass distribution cut pattern 72

LIST OF EQUATIONS

1. Equation 2.1: Natural frequency relationship to stiffness and mass 21

2. Equation 2.2: Flexural stiffness 21

3. Equation 2.3: Mass moment of inertia for rectangular object 21

4. Equation 3.1: Harmonic oscillator 34

ABSTRACT

Micro air vehicles (MAVs) are a useful tool for numerous tasks, such as environmental mapping, search and rescue, and military reconnaissance. As MAV applications require them to operate at smaller and smaller length scales, traditional propulsion mechanisms (e.g. fixed wings, rotating propellers) cannot meet these demands. Conversely, flapping wing micro air vehicles (FWMAVs) can to realize flight at sub centimeter-lengths. However, FWMAVs face design challenges that preclude autonomous flight, including inefficient energetics and reliable on-board sensing. A comprehensive understanding of flying insect biomechanics may provide valuable design insights to help overcome the challenges experienced by FWMAVs. Insect wings have biological sensors that provide feedback to control attitude and wing deformation improves both inertial and aerodynamic power economy. Consequently, the insect wing can guide the design FWMAV-employed artificial insect wings.

The present work aims to (1) dynamically characterize real insect wings via experimental modal analysis, and (2) develop dynamically similar artificial wings to be used on FWMAVs or in controlled studies. To our knowledge, no existing artificial insect wing models are isospectral and isomodal with respect to their biological counterparts. Isomodality and isospectrality imply they have identical frequency response functions and vibration mode shapes, and thus will deform similarly under realistic flapping conditions. We measured the frequency response function and vibration modes of fresh *Manduca sexta* forewings using an electrodynamic shaker and planar scanning vibrometer and estimated the wings' mass distribution via a cut-and-weigh procedure. Based upon our results, we designed and constructed the artificial wings using fused filament fabrication to print a polylactic acid vein structure, based upon the actual vein size and arrangement present in biological wings. Thin polymer films were manually layered over the vein structure and trimmed to fit the wing boundaries to produce a flat wing structure. We determined that the biological and artificial wings have nearly identical natural frequencies, damping ratios, gain, and shape for the first vibration mode. The second mode exhibited complex modal behavior previously unreported in literature, which likely has significant implications to flapping wing aerodynamics. We demonstrate the feasibility of fabricating economical, realistic artificial wings for robotic applications moving forward.

INTRODUCTION

Micro air vehicles (MAVs) have become a prevalent technology in the last decade and can be found in industries such as agricultural monitoring, land surveying, and remote sensing. Many applications require MAVs to be compact so that they may be used in restricted spaces or constrained areas. Conventional fixed-wing or rotor-based MAVs are ill-equipped for tasks in small quarters (less than 10 cm of open space) because they are unable to be scaled down to the appropriate size. At low Reynolds numbers, fixed-wing or rotor generated aerodynamic lift forces are dominated by viscous forces [1]. Furthermore, conventional rotary motors are unable to dissipate heat effectively at reduced length scales [2], which makes them impractical for use on small vehicles. Conversely, flapping wings take advantage of unsteady and quasi-steady aerodynamic mechanisms that can scale down almost indefinitely. As a result, flapping wing flight is the most promising means of propulsion for centimeter scale MAVs [3-9]. Insects present an excellent design paradigm for very small (10 cm or less in dimension) flapping wing micro air vehicles (FWMAVs) due to their size and ability to sustain flight for long periods of time. Insect wings can guide the design of artificial wings employed by robotic vehicles.

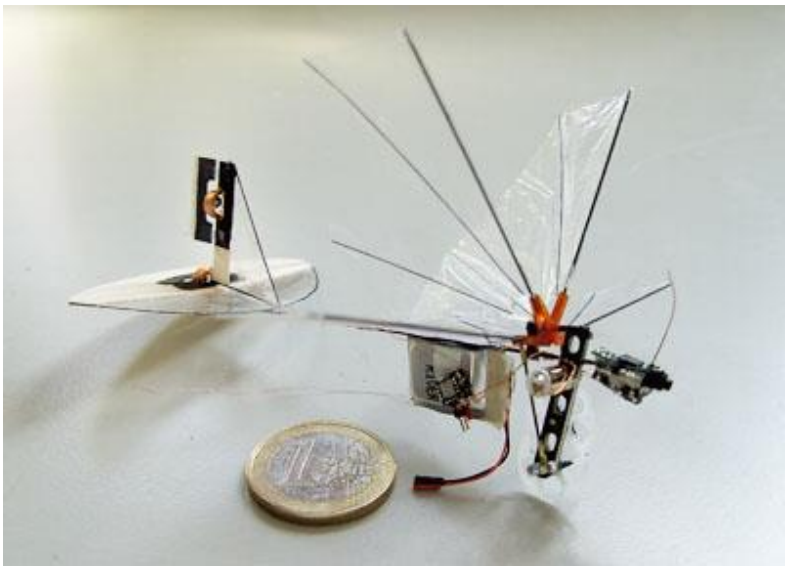

Figure 1.1: Delfly FWMAV produced at Delft University of Technology in Delft, Netherlands. Photo credit [Cdewagter - Digital Camera, the Netherlands (Delft), CC BY-SA 3.0, https://commons.wikimedia.org/w/index.php?curid=30159036].

However, many technical challenges remain in designing and optimizing FWMAVs. Due to their small size, fitting an on-board power supply to a MAV poses a large obstacle to its autonomy. Most MAVs are not autonomous in the sense that their power supply is on-board rather than external because the amount of power required to keep the vehicle in flight for a useful time period is much greater than the power actually required by an insect to keep itself in flight. Designing an on-board power supply that meets the needs of the vehicle while not exceeding the maximum allowable weight is one of the greatest challenges, partially because current bioinspired FWMAV designs simply cannot yet emulate the simplicity and elegance of the natural design. Any design parameters that can be further tuned to close this gap will push FWMAV design closer to an autonomous future.

Background

An important design aspect in realizing this goal is wing structure. However, studying and understanding insect wing structure can be difficult. Insect wings vary between individuals of the same species, which creates obstacles to making repeatable measurements on successive wing samples. Furthermore, studying insect wings in operable condition is difficult because they begin to desiccate immediately after the insect is sacrificed, which allows only a short window of time in which structural data from the wing is viable. Wings are the main driving force of a FWMAV, therefore most of the power demands come from the wing design and its flapping mechanism. It has been suggested that wing flexibility plays an important role in reducing power requirements of flapping wings, therefore understanding the role wing flexibility plays in wing structural dynamics is necessary to improving wing power economy [10]. Understanding the role of structural dynamics in flapping wing flight is of high importance to realize the goal of physical autonomy in FWMAVs.

The structural mechanics of insect wings can guide the design of FWMAV wings. A FWMAV design based on a hawkmoth (Fig. 1.2), for example, could be capable of hover as well as forward and backward flight. Due to the insect's body mass (1.5-3 grams, according to Norris [11]) it is ideal for small scale flight still capable of carrying a small payload, such as a camera. Their wings make up a very small percentage of their body weight (generally less than 5 percent, according to my own wing mass data), which leaves most of the artificial insect body's mass to be used by any onboard flapping motors and power supplies.

Figure 1.2: A *Manduca sexta* hawkmoth is shown with a centimeter scale to demonstrate size.

A thorough understanding of the structural mechanics and dynamics of the insect's wings will guide the most efficient designs of artificial wings. For example, rigid wings have little to no flexibility during flapping and as a result expend more energy than flexible wings during flapping in hover. Single degree-of-freedom experiments on rigid and flexible airfoils have shown that insect wing flexibility may reduce the energetic costs of flight by up to 25 percent via elastic energy storage in the wing and compliant thorax [10]. Properly designed artificial wings will incorporate this flexibility, thereby reducing power consumption. Seemingly small changes such as including the appropriate flexibility will be key in realizing an energy-efficient, physically autonomous FWMAV capable of prolonged flight times.

Insect wings display complexities in vein structure, membrane structure, microstructure, and material properties [12, 13, 14]. A variety of techniques have been used to study insect wings, including micro-computed tomography (CT) scanning, scanning electron microscopy, acoustic microscopy, nanoindentation, tensile testing, and flexural bending tests [15-21]. Static structural studies have provided useful information

on insect wings such as stiffness profiles, mass distributions, flexural data, microstructural characteristics and material properties. In a seminal study done by Combes and Daniel, the pattern of flexural stiffness variation over the *Manduca sexta* forewing was determined [15, 16]. They examined the relationship between venation pattern and wing flexibility by comparing the simulated flexural stiffness of the chordwise and spanwise directions in several insect species via finite element analysis. Their results suggested that spanwise flexural stiffness is 1-2 orders of magnitude larger than chordwise flexural stiffness across all species considered. Furthermore, they suggest that the presence of the leading-edge vein is responsible for the significant anisotropy in spanwise-chordwise bending. They went on to measure wing displacement under a point load applied at either the leading edge or the tip using photographs of the wings illuminated by sheets of laser light during loaded and unloaded states. They used these data and a continuous beam equation to approximate flexural stiffness for each wing. Two finite element models were produced for comparison. The first model has uniform stiffness across the entire wing, while the second model has strips of decreasing flexural stiffness, with the least stiff elements near the wing tip. They found that the model with decreasing stiffness more accurately modeled their findings for flexural stiffness and concluded that stiffness decreases from root to tip and from leading edge to trailing edge. Micro-CT scans performed by Sims, Palazotto, and Norris revealed the wing's natural camber and individual vein geometry [17]. Ma et al. characterized the functional morphology of honeybee wings using scanning electron microscopy, micro-CT scanning, and flexural bending tests [18]. Song et al. measured the hardness and elastic modulus of

cicada wings using nanoindentation [19]. Talucdher et al obtained the tensile modulus and strength of damselfly wing veins via tensile testing [20]. Their work suggests that the average strength (232 - 285 MPa) of the veins they measured is virtually the same in dry and fresh samples. Ennos determined the mass distribution of *Diptera* wings by cutting one into small uniform pieces and determining the wing's mass loss with each cut [21]. Each of these studies contributed valuable information to the study of insect wing physical properties, such as stiffness profile and the effect of the leading-edge vein, wing camber and geometry, hardness and elastic modulus, and a technique for determining mass distribution. These works provide a basis on which to begin understanding the structural dynamics of insect wings, and eventually, to design and build synthetic wings.

While the static mechanics of insect wings have been extensively studied, dynamic mechanics pose a more difficult challenge. Some of the dynamic characteristics of insect wings have been characterized, such as damping ratio, natural frequencies, and mode shapes. Sims, Palazotto, and Norris, Chen et al., and San Ha et al. utilized base-excitation coupled with laser doppler vibrometry to obtain an insect wing's natural frequency, mode shapes, and frequency response function [22, 23, 24]. DeLeon and Palazotto utilized photogrammetry to study the dynamic characteristics of a mechanically actuated hawkmoth wing [25]. These studies provided some of the first dynamic qualitative and quantitative information on hawkmoth wings, giving the scientific community information on natural frequency, mode shapes, deflection magnitude and shapes, and wing damping and a means by which to collect this data repeatably.

Other researchers [8, 9, 26-28] have produced artificial biomimetic or bioinspired insect wings that, in some cases, closely mimic some of the structural characteristics of biological wings. Liu et al produced an artificial cicada wing with biomimetic properties based on geometric and structural data including vein thickness, wing mass, and flexural stiffness profile [27]. Their goal was to determine a range of vein thicknesses within which an artificial cicada wing's veins may be designed so that the wing's natural frequency, flexural stiffness, and strain rate would be similar to that of a biological cicada wing. They produced six artificial cicada wings with identical vein patterns but differing vein thickness and subjected each to mechanical tests to determine the wings' flexural stiffness, maximum deformation rate, and natural frequency. A carbon fiber-based material was used to produce the artificial wing's vein structure, while thin Mylar was used as the membrane. Laser cutting technique was utilized to cut the desired shapes for the wing venation/membrane pattern. Then, the two layers were thermally bonded together to form the completed artificial wing. To maintain the artificial wing's camber, the wing was manipulated during the bonding phase while the epoxy resin used was not yet solidified. Their work suggests a strong correlation between vein thickness and flexural stiffness of the wing. However, their data were compared to a dried cicada wing, and as a result the range of thicknesses they determined were mathematically extrapolated to fit for a non-dried wing. DeLeon and Palazotto [25] developed an artificial hawkmoth wing design based partially on static and dynamic aspects observed by other researchers [15, 16, 29]. The wings were actuated using a custom-made mechanical flapper and photogrammetry was used to capture the wings' deformation at

twelve different angles. Points were mapped onto the wing and followed through the actuation so that their paths could be used to calculate position and deflection. They used this method to compare their synthetic wing to a biological wing and found that the synthetic wing lacked stiffness and exhibited larger deformation than a biological wing during flapping. The synthetic wing's natural frequencies occurred near that of the biological wing, but some differences in response were observed. Sims et al. dynamically excited freshly severed *Manduca sexta* forewings using pseudorandom acoustic signals generated with a signal generator to get their first three natural frequencies and corresponding mode shapes [22]. The wings were sandwiched between thin foam sheets to preserve their natural camber during clamping, and then clamped securely in a clamp that was then mounted on to an amplifier receiving signals from the generator. A scanning laser vibrometer was used to record the wings' displacement and velocity during this excitation. This experiment was done both in air and vacuum (< 4 Torr) to show any differences caused by added mass from the air. They concluded that the first and second natural frequencies of these wings, respectively, is 59 ±2 and 75 ± 2 Hz. Ha et al [28] created an artificial beetle hind wing and performed dynamic and static experiments on it to understand how dynamic and static characteristics are related and to design a characterization method for the dynamic behavior of artificial wings. These works provide a basis from which to continue characterizing insect wing dynamics and to begin perfecting a synthetic wing manufacturing process.

Objectives and Novelty

The aforementioned works have significantly advanced the state-of-the-art in synthetic wing design, however, to the best of our knowledge, no synthetic wing exists that exhibits isospectral and isomodal behavior with respect to its biological counterpart. If a synthetic wing is isospectral to its biological model it exhibits the same magnitude of deflection and velocity when it experiences dynamic vibrations and implies that their natural frequencies are identical, meaning that their frequency response functions (FRFs) are the same. Isospectrality also implies that the damping ratio between the two specimens are the same, which is important for understanding and reproducing a dynamically similar wing. Figure 1.3 shows a vibration spectrum like those which I am comparing between specimens. Likewise, the term isomodal indicates that the vibration mode shapes are equivalent for both biological and synthetic wings. Figure 1.4 shows two different modes for a rectangular plate to demonstrate different patterns of deformation in a vibrating object. Synthetic and biological wings that are both isospectral and isomodal will deform almost identically when subjected to realistic flapping conditions, provided their aerodynamic and geometric characteristics are also similar.

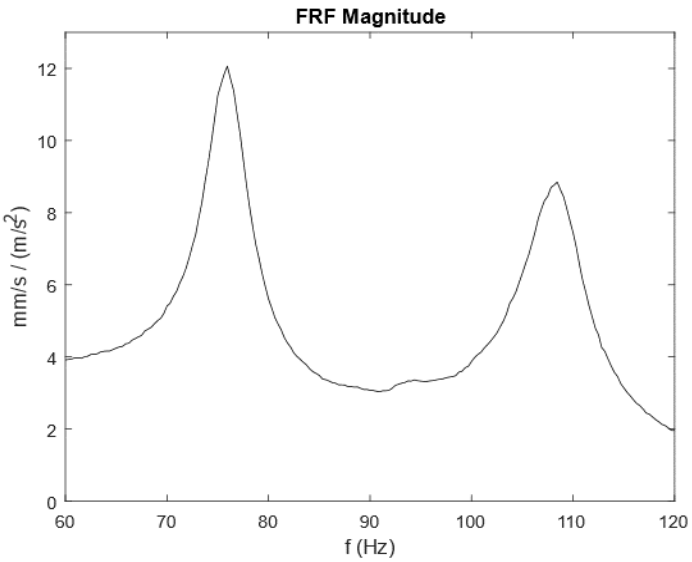

Figure 1.3: A vibration spectrum (FRF) showing two natural frequencies at approximately 76 Hz and 109 Hz. The y axis shows the amplitude of the peak in units of velocity output from the vibrating object per input acceleration via the electrodynamic shaker. Isospectral objects will have identical spectra.

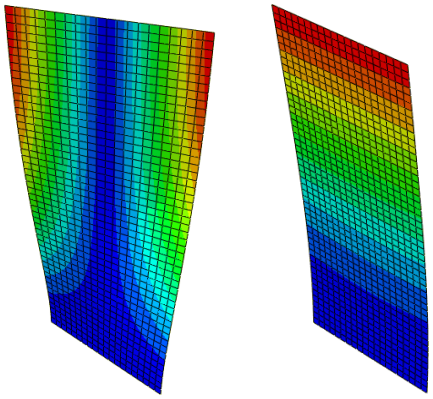

Figure 1.4: Two different modes of vibration in a rectangular plate are shown. When two objects are isomodal they will deform in the same way. The two modes shown are not isomodal.

My work focuses on the first and second modes because they are the most likely to be excited during hawkmoth flight, given that the highest natural flapping frequency is approximately 25 Hz and that the first mode is estimated to occur at approximately three

times this frequency [30, 31]. It has been postulated that the first natural frequency is three times greater than the flapping frequency to offer aerodynamic and energetic benefits to the insect during flight [30, 32, 33]. I believe these benefits occur via excitation of a near-resonant response in the wing at the first natural frequency. At one-third the natural frequency, the flapping frequency may excite an odd harmonic over the wing that causes a large dynamic response near the wing's first natural frequency. The second mode may be excited in much the same way, however the wing visibly experiences torsion during flight, particularly during pitch and angle-of-attack changes [31, 22]. These two modes play very important roles in insect flight, and as such are my primary focus. Successful realization of a dynamically similar isospectral and isomodal synthetic insect wings can significantly improve our understanding of biological flapping wing flight and inform FWMAV design.

The goal of this work is to inform the design and production of a synthetic, dynamically similar insect wing via structural dynamic experimentation and simulation of a real *Manduca sexta* hawkmoth forewing. A successful artificial wing design could revolutionize current FWMAV technology, bringing more efficient and realistic flight to the overall design of FWMAVs. It could also replace biological specimens in some areas of experimental research, thereby freeing researchers from the time constraint that currently accompanies any insect wing studies due to desiccation. More accurate data could be gathered with no time constraint. I chose to focus on the forewing of the *Manduca sexta* hawkmoth for three reasons: (1) a wealth of data exists on the hawkmoth, making it easy to study relative to other insect models; (2) its size makes it a promising

candidate for useful bioinspired micro air vehicles (MAVs); and (3) it is capable of hovering flight, which is important for MAV applications.

I used experimental modal analysis and finite element analysis in the present work to produce experimental and simulated data, respectively, for both synthetic and real insect wings. Our collaborators at Binghamton State University of New York manufactured each of the wing iterations using 3D printing/additive manufacturing techniques. Each iteration was informed by my data on mass distribution, stiffness, damping, natural frequency, and modal response to base excitation that are all detailed in the coming chapters of this document. Parametric studies on the effects of wing curvature, linear tapering of mass in the chord- and span-wise directions, and bilinear mass tapering in both the chord- and span-wise directions were performed to provide tunable models for the parameters observed to be most important to the wing's overall physical structure. All these aspects will provide a robust and clear data set that enables the design and manufacture of a dynamically similar, isomodal, isospectral artificial insect wing.

PARAMETRIC STUDIES TO GUIDE WING DESING

In this section I will detail the methods I used to simulate and test a simplified wing model using finite element analysis (FEA), and results will follow. A simplified wing model was necessary to ensure that both our experimental method and simulation could accurately represent reality for a simplified case in which all parameters are known so that we could move forward with confidence when introducing the uncertainty associated with a biological insect wing in experiments and simulations. The first subsection is devoted to the preliminary experiment I performed to test our experimental setup and FEA model, and the following subsections detail the finite element simulations and other parametric studies I performed to understand how tuning various physical attributes of the wing would affect its frequency response. Our design[1] is constrained by wing mass, size, and planform, given that these are well defined aspects of the insect wing and as such are considered fixed parameters. We therefore had the freedom to adjust mass distribution via thickness variation and curvature to affect stiffness in the wing and influence its dynamic response.

[1]"Our design" refers to the collaborative wing design and manufacture by me, my advisor Dr. Mark Jankauski, and our collaborators at Binghamton State University of New York, Dr. Jia Deng and Huimin Zhou.

Preliminary Base Excitation Tests with a Flat Rectangular Shim

Base excitation and laser vibrometry are commonly used to measure a structure's mode shapes and natural frequencies. Sims et al. used this method to determine mode shapes and natural frequencies of hawkmoth wings [22]. I verified that this method was suitable for my research by testing the experimental setup with a simple structure with relatively little uncertainty in material properties and mechanical behavior. I used a rectangular brass shim with dimensions 5 cm H x 2 cm W x 0.03 cm T, roughly the dimensions of a hawkmoth forewing. I began with this simplified model because I wanted to be certain that I understood the method and was able to use it to confidently to produce expected results. The shim is a relatively homogeneous structure whose material properties are well known and thus should behave predictably. I reasoned that if I was able to produce predictable results using the shim then my experimental setup was likely adequate to apply to a more complex structure such as a hawkmoth forewing.

I tested the shim by loading it into a custom-made clamp with 3.2 mm thick hobby foam on either side so that the shim was sandwiched between the layers when the clamp was fully tightened, as in the work performed by Sims et al [22]. This assembly was loaded into a small electrodynamic shaker (The Modal Shop, K2007E007) capable of producing up to 31 N of force. A periodic chirp signal from 10-1000 Hz with step size of 309 mHz was given to the shaker via an amplifier attached to a signal generator. We chose this frequency range because it contains the shim's expected first and second modes. Data were acquired at 2.56 kHz, which produces a spectral resolution of 3200 FFT lines over the frequency range. This sampling speed allows a high degree of scan

accuracy while keeping the total sampling time under 45 minutes to minimize wing desiccation, which would be important once I began testing wings. A planar scanning laser vibrometer (Polytec, PSV 400) was used to produce a full scan of the shim during excitation, with 15-40 scan points, depending on the resolution I chose at the time of the experiment. The resolution did not appear to affect the shim's FRF notably, so I settled near 30 scan points to balance between scan time and appropriate degree of accuracy. An accelerometer (PCB Piezotronics, 352A21) was affixed to the clamp using mounting wax and was used as the reference channel. The accelerometer was affixed to the clamp so that rigid body motion experienced by the entire assembly could be subtracted from the overall response, so that only the shim's response to excitation would remain once the data were processed in the PSV software. A photo of this setup is shown in Figure 2.1. These data were processed from the time domain to frequency domain via fast Fourier transformation within the PSV software, and an FRF relating base acceleration to wing velocity was output. The mode shapes and natural frequencies obtained from this scan were compared to a finite element model of the shim created in Abaqus (Fig. 2.2).

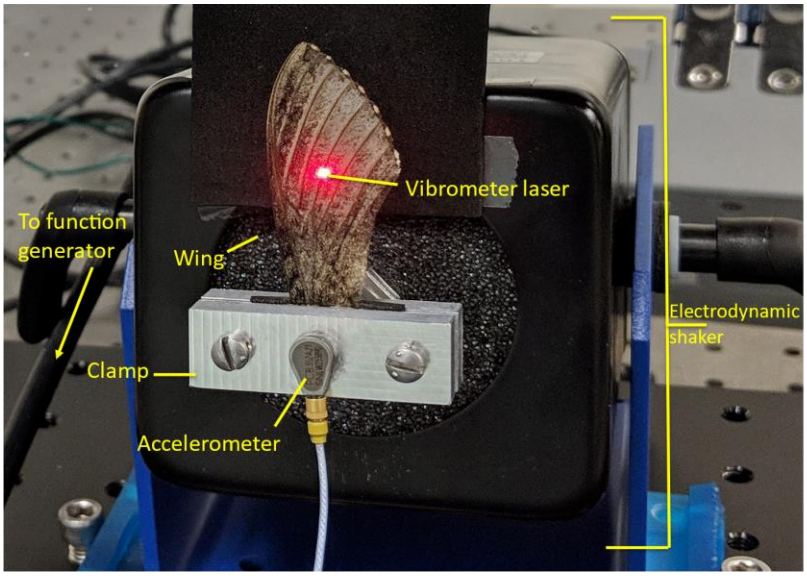

Figure 2.1: The experimental setup with a biological hawkmoth wing loaded into the clamp is shown and labeled. The vibrometer (not shown) is projecting the laser onto the wing from in front of the surface shown.

I performed a series of finite element model analyses on the shim using Abaqus finite element analysis software to predict and understand how thickness variations across the structure would affect its natural frequencies and mode shapes. First, I created a two-dimensional rectangular shell measuring 2 cm W x 5 cm H x 0.03 cm T to match the shim's dimensions. I used the following material properties for this model: $\rho = 8500$ kg/m^3, E = 72.675E9 Pa, and $\nu = 0.33$ where ρ is density, E is Young's modulus, and ν is Poisson's ratio. These values were manipulated slightly from the values shown in [34] to better fit my model. I meshed the part with 1000 linear quadrilateral elements of type S4R, which indicates that the elements are conventional quadrilateral stress or displacement shell elements that use reduced integration to form the structure's stiffness matrix [35]. Reduced integration is used because it reduces running time and produces accurate results for elements that are not distorted or irregularly shaped. I determined that

1000 elements was the appropriate quantity through mesh convergence experiments in which I varied the number of elements from 10^0 to 10^5 and plotted the results of a linear perturbation simulation in MATLAB to determine at what point the result no longer changed. I compared the flat model to experimentally determined natural frequencies and mode shapes for the real brass shim mentioned at the beginning of this section.

My FEA model was able to accurately predict the mode shapes and natural frequencies of the actual shim during testing. My scans of the shim show natural frequencies at 87 Hz and 394 Hz for the first and second modes, respectively, while my FEA model shows 87.86 Hz and 404.05 Hz for the first and second modes, respectively. They also exhibit the same mode shapes at these frequencies (Fig. 2.2). With my FEA model accurately predicting the shim's behavior through the second mode, I moved forward to introduce greater complexity into the model via thickness and camber variations.

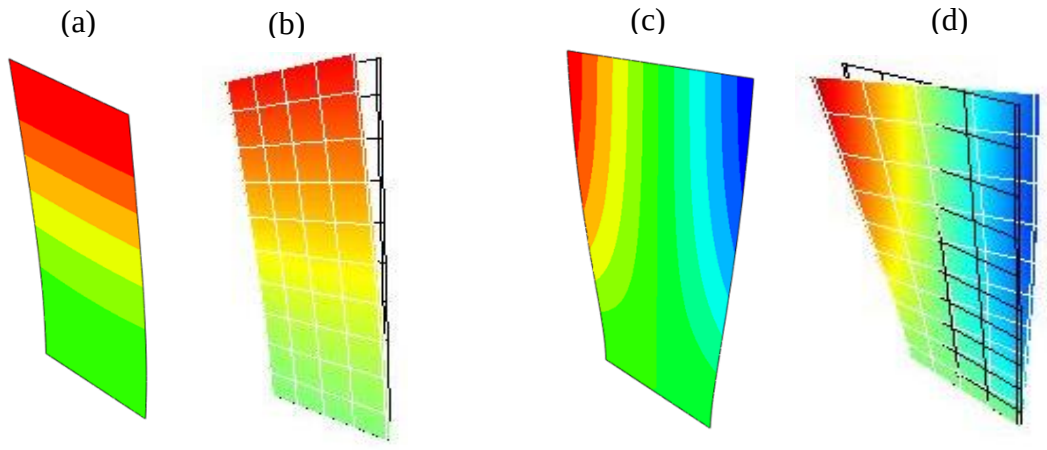

Figure 2.2: The first two mode shapes of the shim represented in FEA (a and c) are shown compared to vibrometer scans of the shim (b and d). The boundary conditions on the shim are clamped-free, where the bottom is clamped, and the rest of the shim is free to vibrate. The first mode takes on a bending shape (a and b) while the second mode is torsional (c and d). In both models, red indicates positive displacement, green indicates little to no movement, and blue indicates negative displacement.

Rectangular Model with Varying Linear and Bilinear Thickness Distribution

Once the model accurately represented the actual shim, I modified the model to exhibit varying mass and thickness distributions as well as curvature to simulate how thickness variations and curvature affect the modal response of the structure. Understanding how these parameters can be tuned to affect mode shapes and natural frequencies will help guide the design of a wing that will bend and deform in a way that emulates a real wing's dynamic response. Mass and stiffness affect natural frequency, but the local values of each can be difficult to discern and are important in overall structural dynamics.

Linear Thickness Variation

Using the analytical field function applied to the rectangle's shape, affecting all elements, I distributed the mass in a decreasing linear path across the rectangle in either the chord- or spanwise direction as shown in Figure 2.3.

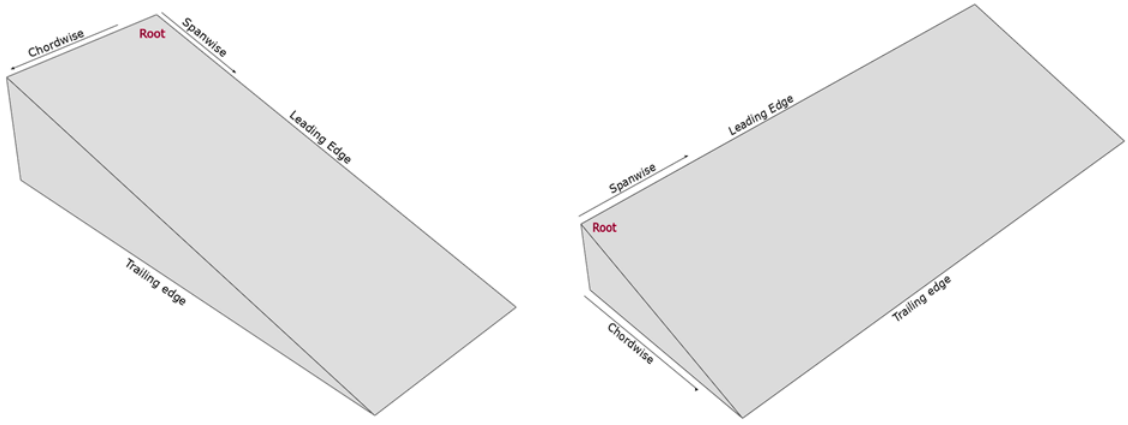

Figure 2.3: Spanwise mass and thickness tapering (left) and chordwise thickness tapering (right). The models shown have pronounced tapering to illustrate the asymmetric distribution of mass and thickness in the finite element models. Spanwise tapering tends toward the root end and chordwise tapering tends toward the leading edge, to imitate the larger mass and stiffness associated with these regions in the actual insect wing.

The mass distribution varies, using step sizes of 10 percent of the total mass, from being evenly distributed across the midline, to all the mass being contained on one side of the axis. For reference, the spanwise midline is located halfway between the trailing and leading edges and runs in the spanwise direction, and the chordwise midline is located halfway between the root and the tip and runs in the chordwise direction. The shape was changed in this way to ensure that the mass and density of the rectangle remained constant and no observed changes in response were due to any factors other than mass and thickness distribution. The mass distribution was only increased moving toward the leading edge or root edge to simply model the mass distribution of the actual insect wing. This was repeated for both the chord- and spanwise directions.

As the chordwise mass distribution goes from a flat and even distribution across the entire plate to having all of the mass being distributed in a tapering fashion from the root edge to the chordwise midline, the frequency response shows the first and second natural frequencies increasing linearly, with the second natural frequency being more dramatically affected than the first. The second natural frequency increases 4.87 times faster than the first natural frequency. In the spanwise direction, both natural frequencies increase with increasing gradation, however the difference between the first and second mode is much less pronounced, with the second natural frequency increasing at a rate of 1.37 times faster than the first natural frequency. These results are illustrated graphically in Figure 2.4.

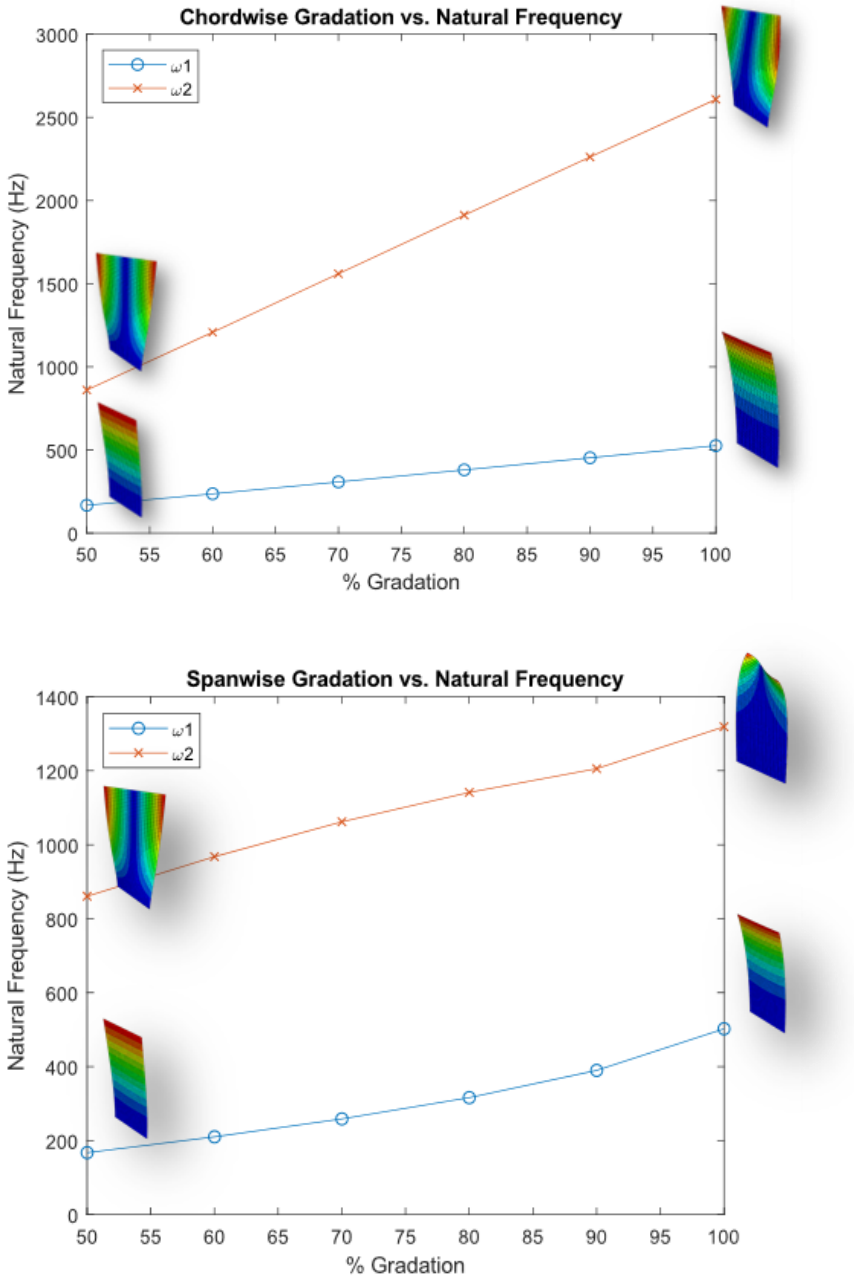

Figure 2.4: The shim's second natural frequency is more sensitive than the first mode to chordwise gradation. This difference in sensitivity is reduced when considering the spanwise direction. The insets show the mode shapes as represented in FEA at the least and most percent gradation across the plate, where 50 on the x-axis indicates a flat shim and 100 indicates the highest degree of mass distribution asymmetry introduced to the model.

These trends are expected, as the first natural frequency corresponds to the first bending mode and the second natural frequency corresponds to the first torsional mode. In a rectangular plate with cantilevered boundary conditions, a torsional mode is more sensitive than a bending mode to chordwise changes in mass because the torsional mode presents as a twist from root to tip, about a spanwise axis.

The side which has more mass is going to cause the entire structure to require more energy to excite the same mode shape due to the relationship between natural frequency and mass:

$$\omega \approx \sqrt{\frac{k}{m}} \tag{2.1}$$

$$k = stiffness$$

$$m = mass$$

The flexural stiffness will increase as thickness increases cubically; mass, however, has a linear scaling relationship to thickness (Eq. 2.2, 2.3).

$$Flexural\ Stiffness = EI \tag{2.2}$$

$$where\ I = \frac{bh^3}{12} \tag{2.3}$$

$$b = base\ of\ rectangular\ cross\ section$$

$$h = height\ of\ rectangular\ cross\ section$$

The localized stiffness is then sensitive to changes in thickness due to varied mass distribution, causing an overall increase in natural frequency. This localized stiffness increase will affect the bending mode as well, but to a lesser degree because the mass and stiffness are unevenly distributed perpendicular to the bending axis. We observed that the spanwise mass distribution variation affects the torsional mode more than the bending mode for rectangular plates of this particular aspect ratio.

Bilinear Thickness Variation

Combinations of thickness variation in both the span- and chordwise directions were created to produce a bilinear thickness gradation to more accurately mimic the multi-directional mass distribution of the actual moth wing. The bilinear gradation was created using an analytical field containing two variables instead of one. Twenty-five bilinear combinations were created to capture each possible combination of chord- and spanwise thickness gradation.

The trend of increasing natural frequency with increasing gradation is present in both the first and the second natural frequencies. The second natural frequency is more sensitive to the bilinear gradation, as its increases at a rate of 2.48 times the first natural frequency. This is as expected because it is between the rates of the individual mass distribution variations. The results of the bilinear thickness gradation can be seen in Figure 2.4.

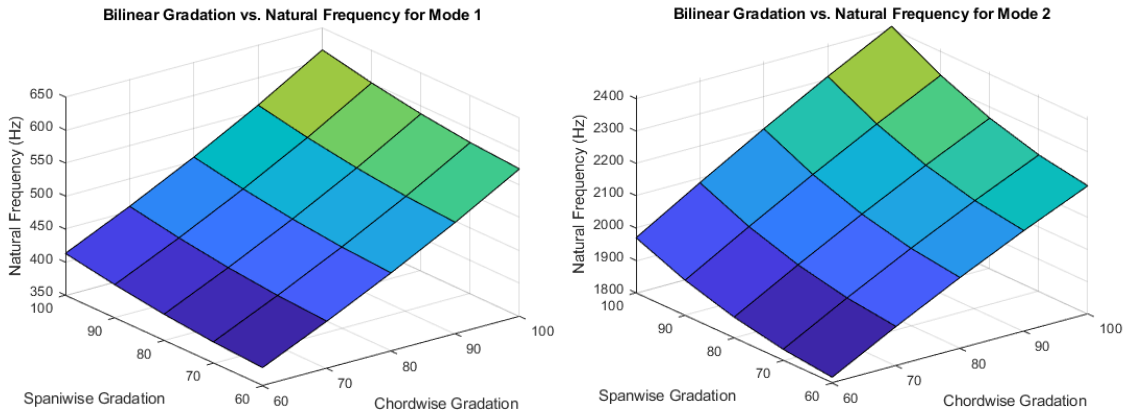

Figure 2.4: A surface plot of chordwise and spanwise percent gradation versus natural frequency of the shim was made for both modes to show how bilinear thickness gradation affects each of the two first natural frequencies. In both images, it should be clear that the chordwise gradation still affects the natural frequency more than the spanwise gradation, but that the highest value for both modes occurs at the highest level of gradation for both directions.

Effects of Camber on a Rectangular Shim

I created the cambered models by using the same flat rectangular plate model used for the flat shim, except I introduced a slight arc in the chordwise direction (Fig 2.5). Arc length was kept constant at 2 cm and the degree of curvature was changed in increments of 2.5 degrees from 0 to 15 degrees in the chordwise direction to introduce camber into the model. I created six cambered models (from 2.5 degrees to 15 degrees) and compared their results to each other and the flat model to show the relationship of camber to the first and second natural frequencies.

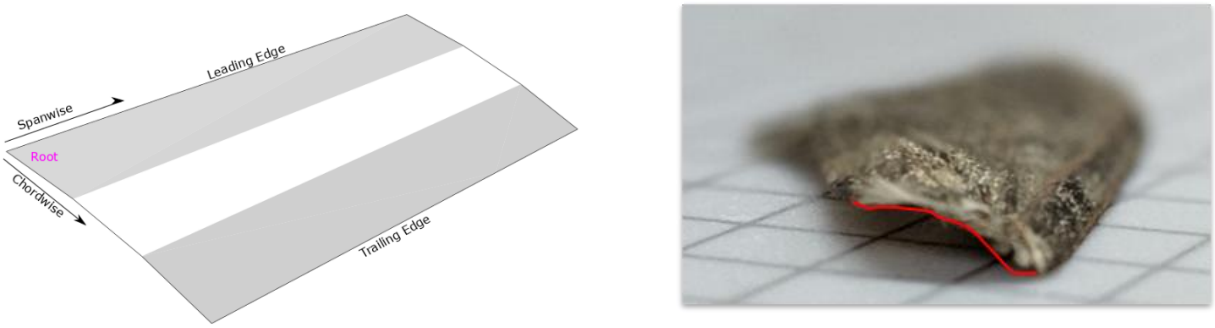

Figure 2.5: A cambered FEA model (left) is used to model the camber in a hawkmoth wing (right). The camber of the actual wing is traced in red.

Varying the camber produces a different trend than that produced from any of the thickness variations. This simulation shows that, as camber increases, so does the first natural frequency, however the second natural frequency is virtually unaffected by the increase in camber (Figure 2.6). Increasing chordwise camber causes an increase in chordwise stiffness. The bending mode acts perpendicular to this increase and so is notably affected by the change, especially relative to the torsional mode, which acts parallel to the spanwise direction. This information may inform design choices related to the degree of camber we choose to introduce into our artificial wing and can help us understand how our artificial wing compares geometrically to the biological wing. I have confidence in my simulations because my parametric finite element simulations show trends that agree with those presented in literature [36, 37, 38].

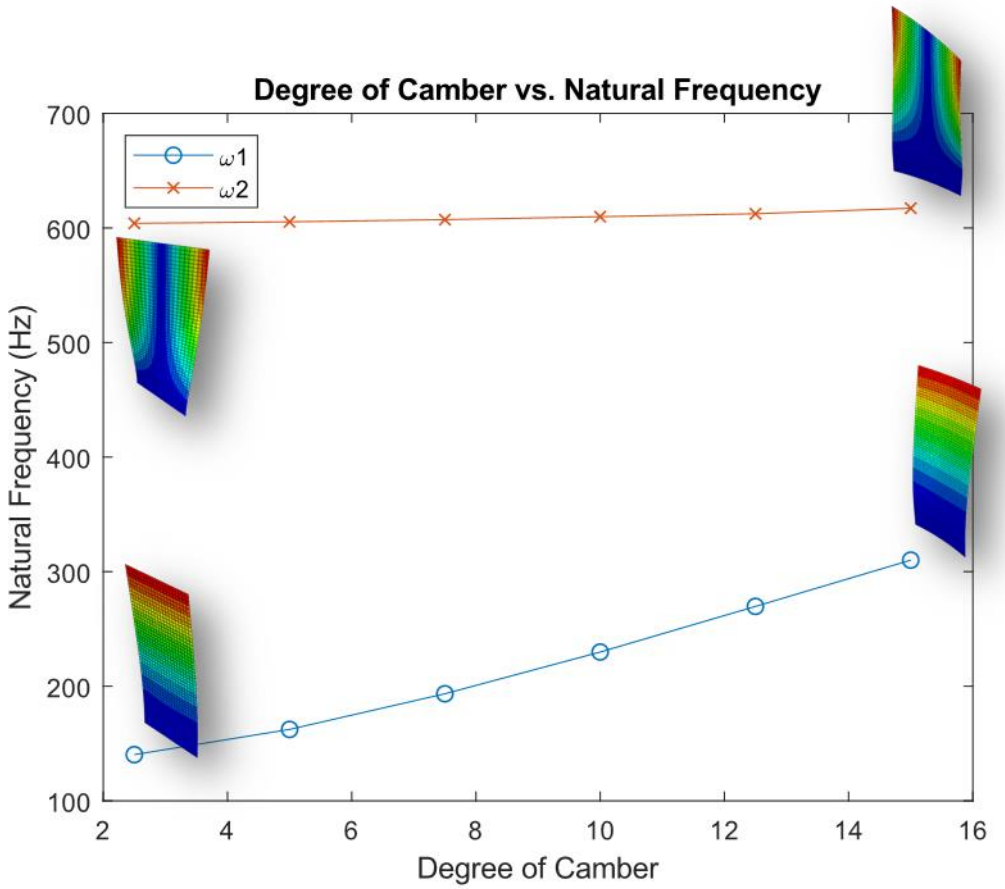

Figure 2.6: The relationship between camber variation and the first and second natural frequencies shows that the first natural frequency is much more sensitive to camber variations than the second mode.

Determination of Mass Distribution

Work by Combes and Daniel [15, 16] suggests that the stiffness profile, which plays a key role in the structural dynamics of insect wings, decreases from root (where the wing attaches to the insect's body) to tip and leading edge to trailing edge, forming a diagonal taper across the wing. We hypothesized that the mass and thickness distribution of the wing should follow this same pattern, so I performed a cut-and-weigh experiment

to determine the mass distribution of a hawkmoth wing. The details of the method I used are based on that in [21]. I determined the mass distribution for one previously frozen hawkmoth forewing that was thawed between two pieces of plastic scaffolding wrapped in a damp paper towel for 30 minutes prior to the cutting and weighing. The plastic scaffolding was present to protect the wings from becoming wet during the thaw. Once the wing was thawed, I placed it on a uniform grid with 5 mm x 5 mm squares and held the wing tightly to the grid as I used a small dissection scalpel to cut the wing along the gridlines. This resulted in thirty-six approximately 5 mm x 5 mm sections from the wing (see App. C). I massed each section individually on a Mettler Toledo XS205 scale accurate to 100 micrograms and mapped their masses and locations on the wing onto a separate wing trace. I then covered the new wing section map in parafilm and placed it back into the freezer to preserve it. We developed a polynomial curve fitting algorithm in MATLAB to create a two-dimensional fit to show mass distribution and determined that the average thickness is 45 micrometers [10]. This average thickness was also estimated and used in FEA experiments performed by Combes and Daniel [16, 29], which therefore lends support our thickness model. The mass distribution I obtained in [10] followed the same path of decreasing stiffness produced by Combes and Daniel, decreasing from root to tip and leading edge to trailing edge; therefore, we moved forward on the wing design under the assumption that the best model would include this diagonal mass variation. The thickness distribution we determined is shown in Figure 2.7. Here, thickness and mass are directly related because a larger vein, which is more massive than membrane and scales, contributes more thickness as well as more mass.

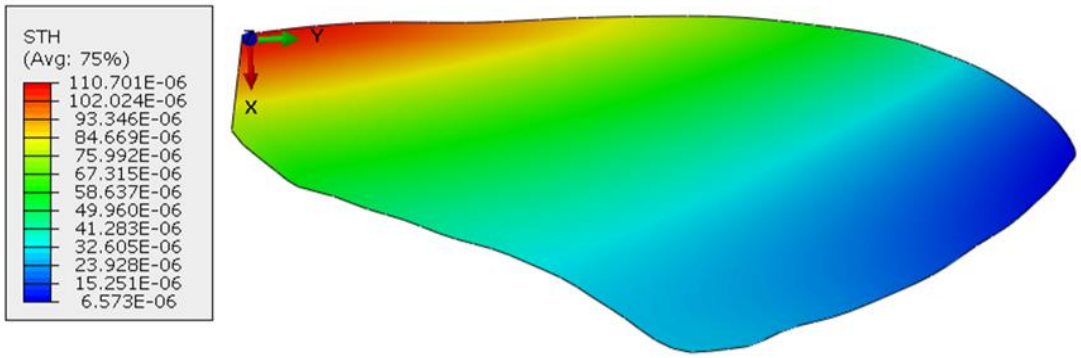

Figure 2.7: The thickness variation is shown as varying from the leading edge of the root to the trailing edge of the tip, with the root being the thickest area. The color bar shown for reference is in meters. This agrees with literature-reported thickness variations [10].

Parametric Studies Summary

These parametric studies provide us with an understanding of how thickness variations and camber variations affect a simplified model of the wing and are supported by literature as mentioned throughout this section. The apparent trends in these data provided a basis from which we began designing our artificial insect wings. The comparison between my scans of the shim and my finite element model showed a reasonable degree of similarity in modal frequencies and shapes, so I proceeded to use this method to characterize the structural dynamics of the more complex insect wing.

DYNAMIC TESTING OF BIOLOGICAL AND ARTIFICIAL WINGS

This section details the dynamic experiments I performed on biological insect wings and artificial insect wings, and the results of these studies. The manufacturing method used to produce the artificial wings is briefly touched upon, but my main contribution with this work is not the manufacture of these wings, so the manufacturing section will be cursory to give the reader a general idea of how the wings were produced.

Dynamic Wing Experimental Preparation

In addition to determining the correct mass distribution and camber, I collected and interpreted dynamic structural data to fully guide the design of a dynamically similar wing. I am interested in only the first and second modes because those are the most likely to show up during flight, as a hawkmoth's wingbeat frequency maximum is around 25 Hz [39]. During flight the first two modes are excited and influence the aerodynamics of the hawkmoth's flight more prominently than other modes might. As a result, the sections involved with dynamic testing of artificial and biological wings focus solely on the first two modes.

Before wing testing could begin, I needed to ensure that I could obtain wings from insects whose sacrifice I could perform, thereby ensuring that the wing sample was as close to that of a "fresh", living sample as possible. The insects were reared on campus by Montana State University's (MSU) entomology laboratory and transported to the Bioinspired Dynamics Laboratory once they reached adulthood and were ready for testing.

Insect Preparation

Manduca sexta larvae were shipped to MSU. Upon arrival at MSU, larvae were relocated to a climate-controlled rearing room at a temperature of 28 ± - 2° C. Larvae were kept in a 24:0 (L:D) h photoperiod to restrict photoperiodically induced pupal diapause [40]. The larvae developed in 0.95 L insect cups with perforated lids and were sustained by Repashy Superfoods Superhorn Hornworm Gutload Diet from Repashy Ventures in Oceanside, CA. Gutterscreen was placed into the cups to provide the larvae a climbing surface.

Each cup contained 3-6 larvae. Larvae were visually inspected for overall health and waste was removed daily. These conditions were maintained for approximately 14-21 days while larvae developed prominent aortae. Once the larvae discontinued feeding, they were relocated to a large Sterilite latching box (23 cm L x 38 cm W x 28 cm H) filled with a uniform 5 cm layer of lightly moist peat soil. Within 48 hours the larvae pupated, and adults emerged after 2-3 weeks. The wings of freshly emerged adults were allowed to fully develop for at least 24 hours before sacrifice. The moths used in this study were mixed gender, with no intentional bias toward either gender so that our model is applicable to hawkmoths in general rather than with a bias towards one gender. Immediately prior to testing, moths were euthanized via a 3.78 L kill jar containing ethyl acetate in a base of Plaster of Paris, in which they remained for fifteen minutes until expiration.

Dynamic Characterization of Biological and Artificial Insect Wings

Dynamic characterization of both biological and artificial hawkmoth wings was performed using identical dynamic procedures to identify their vibration spectra and mode shapes. One biological hawkmoth forewing was removed from the sacrificed moth's body at the wing root using dissection scissors. The remaining wing was left attached to the moth and placed in a refrigerator for the duration of the removed wing's testing, which lasted maximally one hour. Forewings were loaded into the experimental setup detailed in Ch. 2. The clamp holds the wing in place at the root, creating a clamped-free boundary condition. Efforts were taken to create the same position and depth of insertion into the clamp for each wing scanned, to be sure that the tests were performed under reasonably similar boundary conditions. Two strips of 3.2 mm hobby foam were placed on either side of the wing in the clamp to preserve the wing's natural camber, and approximately 3.2 mm of the wing at the root was inserted into the clamp (Fig 3.1).

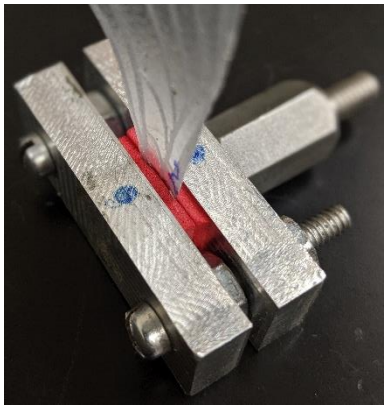

Figure 3.1: An artificial wing is shown in the clamp to demonstrate how camber is preserved. The two foam strips (red) are kept on either side of the inside of the clamp to preserve the camber of the wings.

These steps maintain the wing's natural camber, which is important because camber increases stiffness in some thin structures [37]. This prescribed boundary condition is similar to that used by Sims et al [22]. The method used to dynamically excite and test the hawkmoth wings is the same as for the rectangular shim, since the shim test showed that our method should be appropriate for wing testing. The sampling speed used, 2.56 kHz, allows a high degree of scan accuracy while keeping the total sampling time under 45 minutes to minimize wing desiccation. Larger wings would be assigned more scan points than small wings automatically due to their size. To assign scan points, the scan point feature in the PSV Acquisition software was activated and the polygon feature was used to enclose the region of the wing being scanned. Then, an irregular mesh of density 15 was assigned and scan points were automatically populated within the boundary. This density was chosen because it gave a reasonable spatial coverage and when combined with the sampling rate mentioned above, is still able to maintain a scan time under 45 minutes. The final artificial wing design was also tested in vacuum (< 4 Torr) to remove the effects of added mass from air for a direct comparison to the finite element simulation based on the artificial wing. In-vacuo testing was not a necessary step for the biological wing because we are only interested in the behavior of the wing under realistic conditions, which include normal air density and pressure. The artificial wing is designed based upon data from the biological wings' behavior in air. However, to verify our finite element method with the artificial wing, vacuum testing was necessary to eliminate the need to include added mass in FEA.

The FRF data was then input to the FEMtools Modal Parameter Extractor (MPE) to estimate the wing's first two natural frequencies and their corresponding damping ratios, as well as to display the mode shapes corresponding to the natural frequencies. The MPE extracts modes using a global poly-reference Least Squares Complex Frequency method to identify stable poles in the FRF. Once stable physical poles have been identified, mode shapes with their upper and lower residuals are determined to extract modal parameters [41]. To use the MPE in FEMtools, the file must be in a universal file format, so I uploaded a universal file of the full scan of the wing into FEMtools as a shape file and a data file. Then, I selected the Modal Parameter Extractor addon from the menu bar. I activated the "Extract Poles" tab, and the software assigned a number of poles to use for the extraction. This number may be manually increased if the extraction does not produce poles on the desired peaks in the FRF. Because the FRF data varies from wing to wing, my scans required between 20 and 100 poles to extract modes from the FRFs. Some additional peaks are occasionally extracted and can be discounted if they are not related to modes other than the first or second. Once the desired peaks have been extracted by the MPE, the modes can be stored by using the "store poles" button. Then, in the "Extract Modes" tab, the chosen modes can be extracted using complex or real values, depending on what is required for the desired data. All of the wings used in this research were analyzed using the real extraction tool rather than the complex extraction tool because we are only interested in real modes since the wing is expected to exhibit linear responses with minimal mode shape complexity.

In addition to FEMtools, a custom MATLAB curve fitting script (included in Appendix A.1) was used to further clarify the locations of the natural frequencies. Imaginary and real FRF data were curve fitted using the MATLAB curve fitting script. It is important to use imaginary and real parts of the signal for this curve fit because both the real and imaginary parts of the signal are necessary to estimate the response magnitude and phase of the signal. A phase shift of ±180 degrees indicates a resonance peak, and ideally corresponds to a peak in the complementary signal that shows the magnitude of the response. If the imaginary part of the signal has a phase shift (indicated by a significant peak) at the same frequency as the real part shows a peak, this indicates the real presence of a natural frequency or resonance peak. These data were curve-fitted in MATLAB using three different methods to ensure that all relevant data were captured and fitted in case one curve-fitting method did not adequately capture the appropriate data. Least-squares complex exponential (LSCE), least-squares rational function estimation (LSRF), and peak-picking methods were used to fit the data, and in most cases two of these methods produced very similar results that were close to those observed in the raw data from the vibrometer software. MATLAB uses the least squares complex exponential method to obtain impulse response functions (IRF) from FRF data. It then curve fits a set of complex damped sinusoids to the IRF using Prony's method. The roots of the resulting function are called "poles". The imaginary and real parts of the pole logarithms are determined and used to obtain the frequencies and damping ratios. The peak-picking method assumes that the system behaves like a single degree-of-freedom harmonic oscillator (Eq. 3.1) and that each significant peak in the FRF indicates a mode.

It determines the damping ratio and natural frequencies by setting up and solving a system of harmonic oscillator equations in which mass is replaced by a dummy variable [42].

$$H(f)f_r^2 + j2\zeta_r f_r f H(f) - \left(\frac{1}{2\pi^2 m}\right) = f^2 H(f) \quad (3.1)$$

$H = \textit{frequency response function}$

$f_r = \textit{undamped resonance frequency}$

$\zeta_r = \textit{relative damping}$

$m = \textit{mass of object}$

The Least Squares Rational Function method is similar to the LSCE method, except that it utilizes vector fitting to minimize error. It is best used when the frequency domain is non-uniform. My frequency domains are uniform, so I focused on the results given by peak-picking and LSCE methods. Curve-fitted FRFs show natural frequencies that are generally very similar to the raw values produced in the vibrometer software. Therefore, in cases where two similar sets of peaks are provided, I chose the set that most closely matched those I observed in the raw data. I justify this choice by reasoning that it would be counterintuitive to choose the option that is further away from the raw values, given that the raw values are often reasonably accurate when compared to those produced by curve-fitting.

Before the data can be used in the curve-fitting algorithm, they must be in a format useable to the program. The process to convert this data to a format useable with

this code (comma-separated variable file) is simple but not immediately obvious to a user, so I have detailed it here. The FRF data need to be input into the PSV software's signal processor to convert it to a comma-separated variable file format. To input an FRF into the signal processor, the desired scan must be open and active in the PSV Viewer software. The scan view "Point Data" must be activated. Then, via keyboard shortcuts "ctrl + a" followed by "ctrl + c", the data for each scan point is copied. In the signal processor window, the user selects a cell and pastes the data into the cell. Then, on the menu strip of the signal processor viewer window, a data type can be selected. I selected "Imag and Real" for the purposes of these curve fits. Then, from the software's main menu bar, I selected "File", "Export" and finally "ASCII" for the format. The software then asked for a save location and the document was saved as a Windows 97 Excel file. I then opened each file separately in Microsoft Excel and saved it as a .csv file. The file was now useable with our MATLAB script. The same procedure was repeated for all wings of interest.

Dynamic Biological Wing Data

The average natural frequency we report for the first bending mode is higher than those shown by Sims et al., whose work on dynamic modes of hawkmoth wings is currently the benchmark to which I measure my own data. The comparison between our average values and theirs is shown in Table 3.1.

Table 3.1: My data (left 3 columns) is compared to that presented by Sims et al. (right two columns). My first and second natural frequencies are approximately 16 Hz and 18 Hz higher than theirs, respectively. However, our modal damping ratios are within 1 percent of theirs.

n=5	**Average**	**St. Dev.**	**n=47 (Sims et al.)**	**Average [22]**
Mass (mg)	27.20	2.64	**Mass (mg)**	51.62
W1 (Hz)	75.77	11.46	**W1 (Hz)**	60
Gain (mm/s/(m/s^2))	20.59	12.52	**Gain (mm/s/(m/s^2))**	--
Damping %	4.73	0.44	**Damping %**	5
W2 (Hz)	102.10	12.55	**W2 (Hz)**	84
Gain (mm/s/(m/s^2))	5.37	4.74	**Gain (mm/s/(m/s^2))**	--
Damping %	4.04	1.45	**Damping %**	5

Our damping data is within one percent of theirs and we therefore consider it reliable. However, the wings shown in their work are all more massive than our wings. Looking to the relationship between mass and natural frequency (Eq. 2.1), where natural frequency scales with mass and stiffness, our natural frequencies being higher than those reported by Sims et al. [22] is expected. To verify this I used Eq. 2.1 to calculate the average stiffness of the wings I measured, and then used that stiffness in the same equation with the average values given in Sims et al. to determine whether, assuming the same stiffness, our results compared reasonably with theirs. Using our average stiffness with their data, I obtained a first natural frequency value of 54 Hz, which is reasonably close to their actual 60 Hz average and serves to validate our results for smaller wings.

Dynamic testing revealed the first two mode shapes, frequency response functions, and natural frequencies of the biological hawkmoth wings tested. The

second mode shape and natural frequency of these wings were more difficult to discern, and I will speculate on why this may be at in the last section of this chapter. On average, the wings' first natural frequency, which presents as a bending mode (Fig. 3.4, shown at the end of this chapter), occurred at 75.77 Hz with an average gain amplitude of 13.77 mm/s/(m/s^2) and a damping ratio of 4.7 percent. The average mass for these wings was 27.2 mg. Table 3.2 (pg. 41) shows a comprehensive statistical data set for all fresh and artificial wings scanned.

It is important that we were able to replicate the first bending mode because it appears to be related to the most efficient flapping frequency. The insect's maximum wingbeat frequency reaches approximately 25 Hz, which is roughly one-third of the wing's observed first natural frequency. It has been suggested that this relationship is aerodynamically beneficial and energetically conservative [30, 32] because a near-resonant wing response is potentially being excited at this frequency that allows such energy savings [10]. With the dynamic behavior of the wings known, we developed artificial wings and compared them dynamically to the biological wings.

Artificial Wing Manufacture

Wing manufacture was performed at our collaborator's laboratory at Binghamton University in New York State. First, a vein structure was designed based on collected data from a biological wing and printed from polylactic acid (PLA) using fused filament fabrication. The artificial wing's veins have varying thickness based upon the mass distribution determined through my cut-and-weigh experiment and further refined and

informed by the results of my parametric studies on thickness distribution. The wing design underwent several design iterations (Fig. 3.2) informed by my parametric studies and dynamic characterization of each new batch of wings.

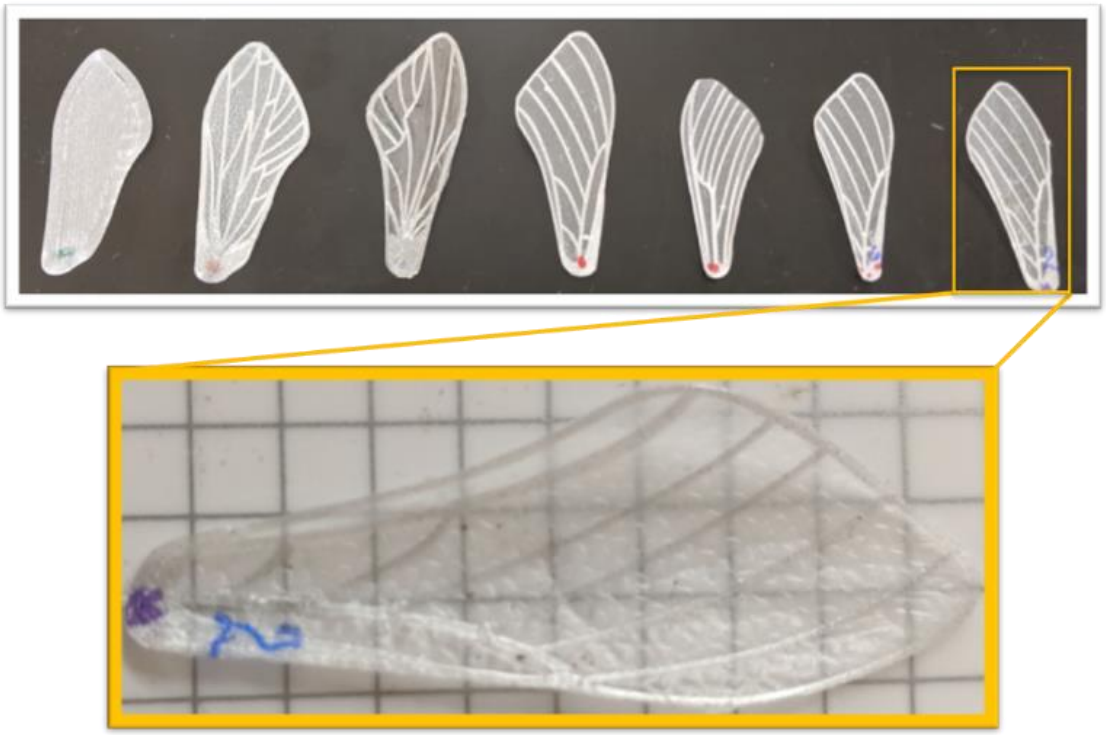

Figure 3.2: Wings from each new design iteration are shown in chronological order from left to right (top photo). The first design incorporated 3D printed carbon fiber. Following iterations incorporated more realistic vein structures and other materials, such as the PLA vein structure and LDPE membrane material used in the final design (bottom photo/far right in top photo).

Our current design employs varying thickness near the root such that the main vein structure would be 0.10 mm, the middle vein structure near the root and leading edge would be 0.20 mm, and the thickest part at the root would be 0.30 mm. These measurements kept the mass of the wing within an acceptable range compared to biological wings while still creating noticeable variation. Figure 3.3 shows an exploded

view of the pieces of the vein structure and membrane with thickness values from one of the artificial wings whose dynamic characteristics best match the average dynamic characteristics of the biological wings.

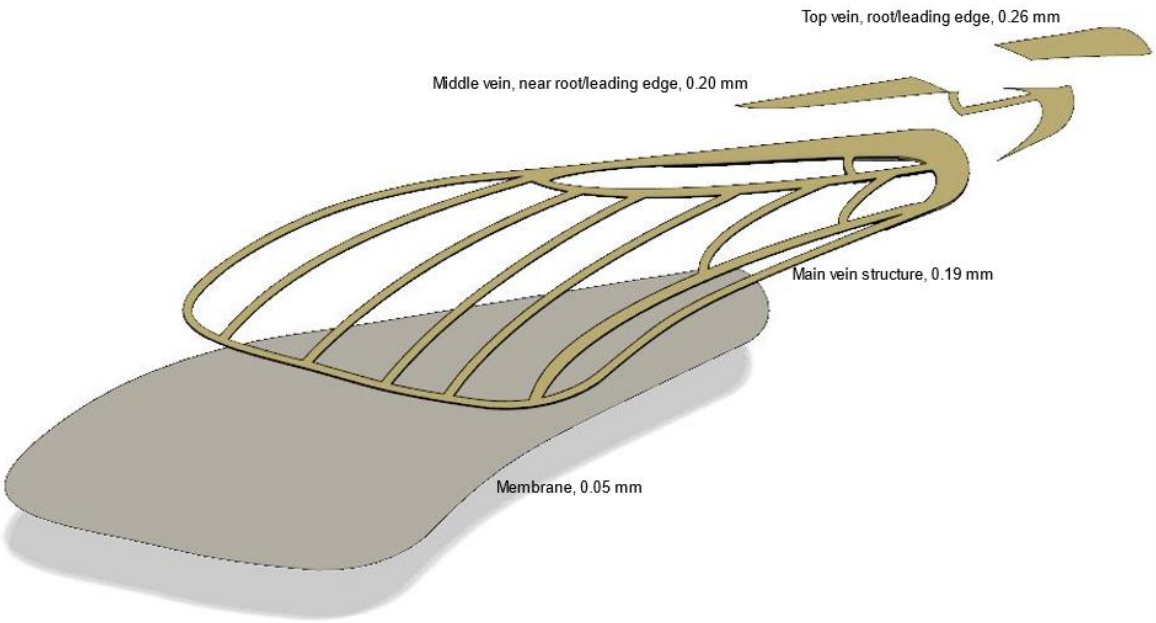

Figure 3.3: An exploded view of the individual pieces used to create the vein structure and the membrane for the FEA wing model. The top and middle veins were assigned greater thickness to model the thickness increase near the leading edge and root of the wing. The thickness measurements next to the part labels were taken from the flat artificial wing. The main vein structure was designed to be 0.10 mm, the middle 0.20 mm and the top 0.30 mm, however some variations exist in the actual wings, so the FEA model was adjusted to reflect this variation.

A thin polymer film was cut to fit the wing's area to emulate the membrane. The combined membrane/vein structure was placed in a 3D printed mold and heated using joule heating to create curvature to match the biological wing's natural curvature. A 3D scan of the wing was used to model the camber, and any changes made to the resulting camber were informed by the results of my camber variation

study, dynamic characterizations, and further manipulation of the wing model in FEA.

In addition to the cambered wings, a set of flat wings was produced so that I could verify my finite element model of the artificial wing before introducing the uncertainty into the model via curvature.

Comparison of Biological to Artificial Wing Response

Nine artificial wings were tested in a test setup identical to that used for the biological wings, and their vibrational responses were compared quantitatively as well as qualitatively. An artificial wing will be considered successful if its natural frequency is within one standard deviation of the average natural frequency for the biological wing set. An artificial wing can be successful in one mode and not the other, although this is not ideal and would indicate that further study is needed to match both modes. We did not design these wings with preference for obtaining one mode over the other, both modes were sought simultaneously. The data collected for both experiments is presented in Table 3.2. The artificial wings' average first natural frequency occurred at 74.96 Hz with a gain amplitude of 15.38 mm/s/(m/s^2) and damping ratio of 0.0256. This is less than 1 Hz difference compared to the biological wing. The second natural frequency occurred at 114.11 Hz with gain of 10.70 mm/s/(m/s^2) and damping ratio of 0.0256. This is 16.55 Hz higher than the observed natural frequency in the biological wing. While this is somewhat significant and is outside of the standard deviation of both the biological and artificial wings, it is not unexpected considering the uncertainties present in the second mode of the biological wing. I processed the FRF data of one artificial wing and one

fresh wing in MATLAB to isolate their first modes for a clear side-by-side comparison.

The resulting plot is shown in Figure 3.4.

Table 3.2: Statistical data on the first and second natural frequency for biological and artificial wings tested in air.

Wing #	Mass (mg)	Area (cm^2)	Span (cm)	Chord (cm)	ω_1	Gain	Damping %	ω_2	Gain	Damping %
Artificial										
In air										
1	43	6.04	4.96	1.84	84.33	17.162	2.49	127.55	7.31	3.51
2	45	6.04	4.96	1.84	76.49	14.786	2.56	103.19	11.244	2.04
3	45	6.04	4.96	1.84	82.47	15.936	2.34	106.37	12.159	2.23
4	42	6.04	4.96	1.84	77.22	12.749	2.6	112.19	8.111	2.46
5	43	6.04	4.96	1.84	82.01	11.839	2.25	133.57	15.136	2.58
6	41	6.04	4.96	1.84	61.58	15.635	3.13	133.59	12.337	1.96
7	43	6.04	4.96	1.84	63.17	25.32	2.14	98.45	11.781	3.4
8	39	6.04	4.96	1.84	76.08	12.062	2.69	108.09	8.848	2.57
9	37	6.04	4.96	1.84	71.25	12.91	2.83	103.98	9.391	2.28
Averages	42.00	6.04	4.96	1.84	74.96	15.38	2.56	114.11	10.70	2.56
St. Dev.	2.49	0	0	0	7.71	3.93	0.29	12.93	2.34	0.52
Biological										
1	31	6.43	4.53	2.02	55.16	21.812	5.18	79.61	2.931	3.04
2	28	5.86	4.67	1.85	85.58	44.212	4.27	102.79	14.73	1.97
3	26	5.39	4.38	1.82	73.12	12.849	4.6	113.87	1.961	4.6
4	23	5.06	4.19	1.71	78.1	15.113	4.3	113.92	2.983	6.22
6	28	5.9	4.78	1.82	86.89	8.984	5.32	100.32	4.257	4.38
Average	27.20	5.73	4.51	1.84	75.77	20.59	4.73	102.10	5.37	4.04
St. Dev.	2.64	0.47	0.21	0.10	11.46	12.52	0.44	12.55	4.74	1.45

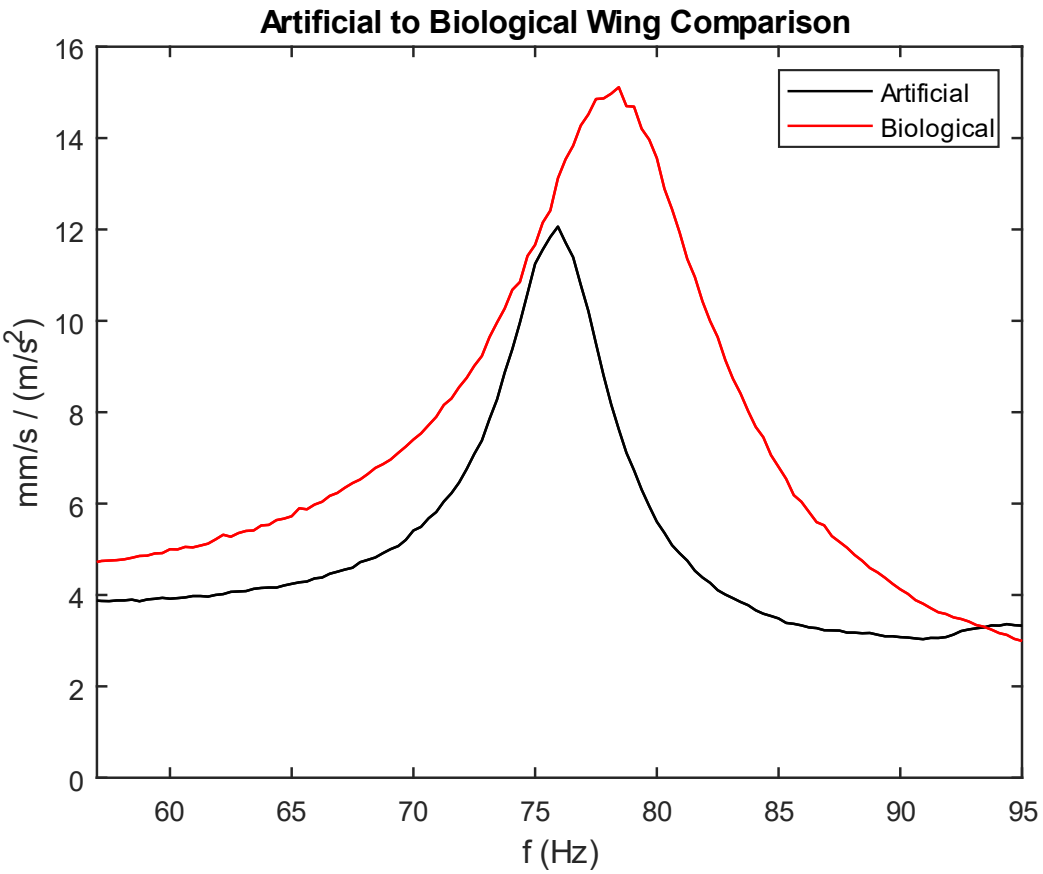

Figure 3.4: First mode frequency response functions of the artificial wing (black) and biological wing (red). The artificial wing's first natural frequency occurs at 76.08 Hz with a magnitude of 12.062 mm/s/(m/s^2) and the biological (fresh) wing's first natural frequency occurs at 78.10 Hz with a magnitude of 15.113 mm/s/(m/s^2).

The first natural frequencies for the wings shown above differ by less than 1 Hz and the magnitudes differ by approximately 3 mm/s/(m/s^2). This difference is less than 10 percent of either wing's first natural frequency and is within one standard deviation of the mean values. Furthermore, their FRFs have the same shape up to this mode. The mode shapes of each at the first natural frequency are compared for similarities in bending and locations of more or less bending relative to each other. Our artificial wing bends in much the same way as our biological wing, as shown in Figure 3.5. Combining the bending

shapes with the numerical data we obtain from the scans allows us to determine how similar these scans are. Figure 3.5 shows the modal behavior of the first bending mode of an artificial wing and a biological wing as rendered by the scanning laser vibrometer.

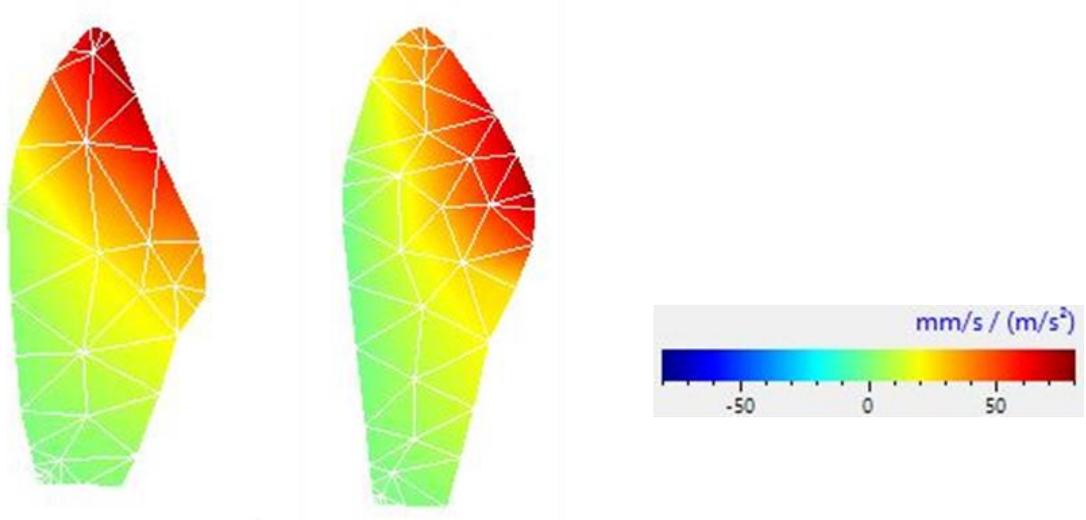

Figure 3.5: The first bending modes of the biological wing (left) and the artificial wing (right) are shown between the biological wing (left) and the artificial wing (right). The color bar indicates the local velocity in mm/s per input of acceleration in m/s^2. In this figure, the tip is represented coming out of the page while the base is essentially held neutral in the clamp.

The spectral and modal data for the first mode of the artificial wing suggest isomodal, isospectral behavior relative to the biological wing is attainable. The second mode's spectral data shows more variation. More research will be required to understand the biological wings' second mode and to make the artificial wings match this behavior.

Results and Discussion on the Second Mode

The second natural frequency and first torsional mode of the wing has a marked effect on the wing's pitch and angle of attack during flight [43]. However, it proved more difficult to separate from other sources of noise in the FRF than the first mode. I was able

to use the same curve fitting algorithm to estimate the second mode's occurrence near 97.56 Hz with an average gain of 3.456 mm/s/(m/s^2) and damping ratio 4.0 percent (for the full second mode data set for real and artificial wings, refer to Table 3.2). Our second mode shows some torsional characteristics, but the dynamic wing shape we observed associated with our wings' second mode indicates that the second mode may be complex, meaning that its FRF has an imaginary component and that differences in damping across the wing affect this mode more prominently than the first mode. A complex mode becomes apparent when phase differences are not static. In a normal mode, the phase of each measurement point is constant relative to all other measurement points. In a complex mode this phase shift is less obvious and the relative positions of elements within the object change in a periodic fashion that makes a still-frame image of the mode difficult or impossible to render.

Insect wing dynamic modal testing literature appears to be lacking the observation of a possible complex second mode in insect wings. It may be that others have made simplifying assumptions in their work or processed their data in a way that unintentionally overlooks this complexity to make experimental wing data fit more closely with the simulation data. Further investigation will be needed to confirm that the wing does, in fact, exhibit varied local modal damping, leading to complex modes, however my data suggest varied local damping leading to complex modes. Varied local damping may affect the second mode (expectedly the torsional mode) more than the first mode (bending) because it has different aspects of the wing's structure contributing to its damping, as it is not a symmetrical or homogeneous structure. Further testing will be

needed to support this argument. There is also a persistent peak in the FRF near 102 Hz on nearly all fresh wing specimens. This persistent peak may indicate an issue within the system or boundary conditions present during the biological wing tests. The shaker head that attaches to the clamp as well as the full test setup with the clamp in the shaker but without the wing has been tested to investigate if this peak is potentially coming from within the testing setup, but the peak was not present in the test setup in these tests. It seems unlikely that such a consistent error would be an intrinsic property of the wing, therefore this error will need to be resolved going forward so that we may confidently show where the actual second mode is located and how it presents across the wing.

From the data presented in Table 3.2 it is apparent that the average mass of the biological wings is lower than the artificial wings. It might seem that, given the relationship mass has to natural frequency that, our artificial wings should have a noticeably lower average natural frequency than the biological wings. However, there are other differences between the biological wings and the artificial wings that may be responsible for their average first natural frequencies being so similar. It is likely that the artificial wing is slightly stiffer than the biological wing, which could drive the natural frequency of the artificial wings up, more towards that of the lighter biological wings. This difference in stiffness may be due to the materials used to produce the artificial wing, the degree of camber, or the vein structure. The stiffness of the wing may benefit from redistributing more of the thickness towards the trailing edge, or from increasing the degree of camber slightly. Looking to my parametric studies, the wing could also potentially benefit from designing systematically for one mode and then the other, for

example by first obtaining the second mode via a flat wing with tapered thickness and then introducing camber to obtain the second mode.

FEA MODELING

The finite element model I present in this chapter is based upon our artificial wing and can be adjusted and modified to inform future design iterations. Moving forward, it may also be integrated with predictive flapping-wing fluid-structure interaction (FSI) models to estimate how the artificial wing would deform under realistic flapping conditions.

Artificial Wing Finite Element Model

Our collaborators produced a CAD model of the artificial wing's veins using AutoCAD's Fusion 360 software. I imported this model into SolidWorks, where I removed all faces excluding those that modeled the topology of the wing's thickness distribution, leaving only a topological model of the wing. I then imported this model back into Fusion 360 produced a trace of the wing's perimeter to model the printed wing's membrane structure. I saved these models individually as Initial Graphics Exchange Specification (.iges) files and imported them as parts into Abaqus. Refer to Figure 3.3 for an exploded view of the CAD model used to create the wing. I modeled wing veins and membrane as separate bodies so that appropriate material properties could be applied individually to each. In Abaqus, I assigned each part its own instance and then translated the instances to be overlaid and just touching, to model the real artificial wing as closely as possible. I used the tie constraint feature to connect the veins to the membrane, ensuring that the tied nodes moved together under excitation, and exhibited responses as one continuous part. There are three separate sections of the vein structure, a

top, middle, and bottom section. The vein model was made in this way to allow discrete thickness changes in each section. Tie constraints were used to connect first the bottom vein section to the membrane section, with the membrane being the master surface and the vein being the slave. The next two sections were tied to the vein section directly below them in the same way, with the lower vein being the master surface. I modeled the wing's vein material as PLA with $\rho = 1.25$ g/cm^3, $E = 3.5 \times 10^6$ Pa and $\nu = 0.45$. I modeled the membrane material as LDPE with $\rho = 0.917$ g/cm^3, $E = 2 \times 10^5$ Pa and $\nu = 0.5$ [44, 45]. Then, I combined veins and membrane into one body using tie constraints on all available nodes. Once the simulated wing was fully assembled, I created four copies of this model with increasing quantity of elements from the order of 10^2 to 10^4 elements and created and submitted a job file for each in which the model was subject to linear frequency perturbations. The first and second natural frequency values were plotted against mesh size and the point at which the response ceased to change was determined to be the appropriate mesh size. Using this method to determine mesh convergence I determined the appropriate mesh size to meet convergence criteria to be on the order of 10^3 elements. I assigned 5,437 shell elements to the model because this quantity is nearly in the middle of this range. Camber was then introduced into the flat model via a curvature point field that we designed using MATLAB (App. A.2) based directly on the actual curvature mold used to create the artificial wing. I imported the curvature into the Abaqus input file and mapped the flat model onto the points accordingly. Both the point field and the flat vein model were designed directly from digital renderings of the artificial wing, and as such would be designed to the same surface area, which also serves to prevent surface area

changes that may occur from mapping the point field onto the flat model. The wing was modeled as a cantilevered plate with the wing root as the clamped edge, as in the dynamic testing. The lower 3.175 mm of the wing (root end) was clamped “Encastre” and the entire model was subject to simulated linear frequency perturbations. This produced simulated mode shapes and natural frequencies for comparison to both physical models.

I began designing finite element models of the artificial wing starting with just a flat model of the veins and membrane. Curvature introduces another layer of uncertainty into the model, so I wanted to be sure my model would first accurately represent a flat artificial wing before introducing curvature. I will briefly focus on the results of the flat model before moving onto the full, cambered artificial wing finite element model.

Flat Wing Model

The flat finite element model showed the first bending mode at 26.424 Hz and the second mode at 99.885 Hz, which is very close to the experimental results, which show the flat wing’s first bending mode in air occurring at 24.962 Hz and the second mode/first torsional mode occurring at 92.624 Hz. They also exhibit very similar mode shapes, as shown in Figure 4.1.

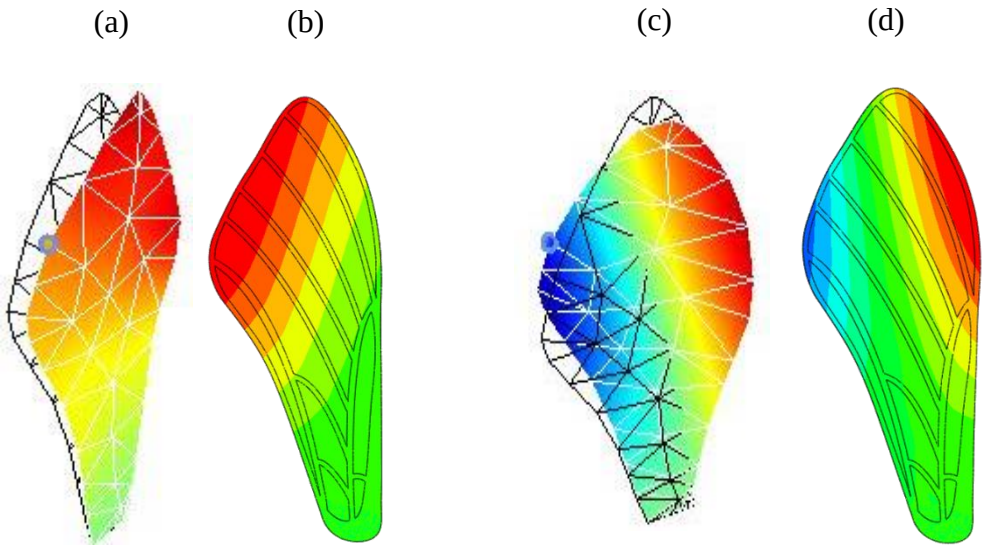

Figure 4.1: The mode shapes of the flat wing rendered by the vibrometer (a, c) are compared to those obtained in FEA (b, d). Bending modes (a, b) and torsional modes (c, d) are shown. The scans of the physical wing are shown next to their static states (black meshing outside of bent wing) to show their movement patterns. In both models, red indicates positive displacement, green indicates little to no movement, and blue indicates negative displacement.

Although these frequencies did not increase substantially when the wings were tested in vacuum, the results from the in-vacuo experiment are even closer to the simulated wing's response, showing the first mode at 27.162 Hz and the second at 94.594 Hz. We expected the in vacuum tests to more closely match the finite element model because we chose not to include added mass from air in our simulation to minimize uncertainty. These results showed that our model of the veins and the membrane and the way in which they are connected accurately represents reality for the flat wing, so I introduced camber into the model at this point.

Cambered Wing Model

When the camber was introduced into the model, the first bending mode occurred after the first torsional mode/second overall mode. This order does not present in the

experimental results for this wing, nor is it predicted from the behavior shown by simplified wing models such as the rectangular plate. We hypothesized that the FEA model's curvature may have been more pronounced than in the artificial wing as a result of material cooling after the membrane heat treatment step during manufacture, since it is unlikely that a model is identical to its mold. I tested this hypothesis by scaling the curvature to be less pronounced than in the original point field and found that the optimal curvature is 79 percent of the modeled curvature. I arrived at 79 percent by an iterative process in which I scaled the curvature by various ratios until the natural frequency values very closely matched experimental values. The in-vacuo experiments were used as the benchmark for this simulation because finite element modeling does not allow the option to include added mass from aerodynamic effects. In-vacuo results show the average first natural frequency at 78.28 Hz and the second at 122.19 Hz, and the finite element results show the first frequency at 78.31 Hz and the second at 121.58 Hz. Both of the first natural frequency values given by my finite element analysis are less than 1 Hz away from the experimentally observed average, and both mode shapes are isomodal with respect to the real artificial wing (Fig. 4.2), which suggests this model is able to accurately model the behavior of the artificial wings. This model can easily be modified to fit any future changes to closer match any new biological wing results.

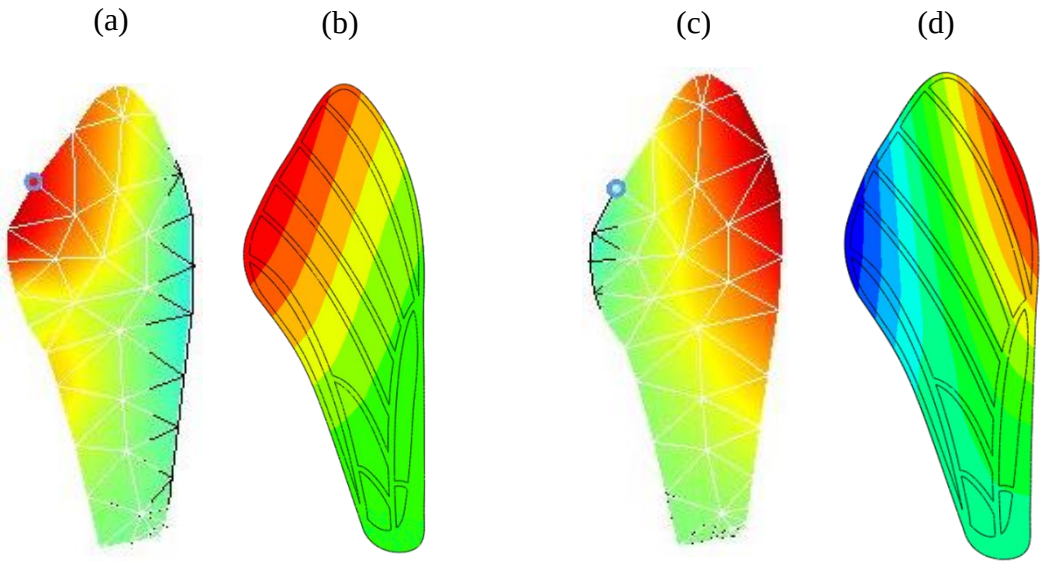

Figure 4.2: The mode shapes of the artificial wing as rendered by the vibrometer (a, c) are compared to those obtained in FEA (b, d). Bending modes (a, b) and torsional modes (c, d) are shown. The scans of the physical wing are shown next to their static states (black and white meshing on deformed wing) to show their movement patterns. In both models, red indicates positive displacement, green indicates little to no movement, and blue indicates negative displacement.

CONCLUSION

To design better, more efficient bio-inspired MAV technology, the scientific community should look to insect models for inspiration. However, proper utilization of insect models requires that we have a better understanding of insect wing structural dynamics. I focused my research on dynamically characterizing *Manduca sexta* hawkmoth wings via modal analysis and FEA methods. Then, with help from our collaborators at Binghamton State University in New York, we designed artificial insect wings based on these data and tested them for comparison to their biological counterparts. Finally, I produced a functioning finite element model of the final artificial wing design that is accurate with respect to modal tests performed on the physical artificial wing.

My parametric studies provided a useful basis on which to inform design changes for thickness distribution and wing camber. The mass distribution I obtained shows that the thickness of the wing decreases from root to tip and from leading edge to trailing edge, which is the same pattern observed in the stiffness distribution obtained by Combes and Daniel [15, 16]. The finite element models I produced based on this thickness distribution showed that increasing degree of thickness tapering across the wing would cause both modes to increase. Increasing the degree of camber in the wing caused a notable increase in the first natural frequency but virtually no change was observed in the second natural frequency. The changes in mode shape I observed in these tests, along with the natural frequency increases, are supported by experimental and theoretical examples in literature [36, 37, 38], therefore I am confident that my FEA methods are

accurate to model changes in the actual wing and influence design decisions. These data combined with the dynamic characterization of the biological hawkmoth wing provide a reliable basis on which to design isomodal, isospectral, dynamically similar artificial wings.

I performed a dynamic characterization of the first two modes of the hawkmoth forewing in terms of natural frequency, mode shape, and associated modal damping. My results were in accordance with those presented in literature [22], however our wings showed some variation in size and mass. We obtained the first mode easily, but the second mode has proven more difficult to isolate, due to the likely presence of previously undocumented complex modal behavior. Our artificial wings do not exhibit this complex modal behavior, and as a result more accurately capture the first mode than the second. The artificial wings' average first natural frequency is within one standard deviation of the biological wings' in damping, gain, and numeric value, as well as mode shape. The vibration spectra and mode shapes are very similar through the first mode. However, the biological wings' second mode will require further investigation to influence future design iterations concerning this mode.

As a consideration for future artificial wing designs and use with fluid-structure interaction simulations, I produced a finite element model of the artificial wing. I first tested it using a flat wing, and then introduced camber once I was confident that it accurately modeled the flat artificial wing's in-vacuo scans. Once the artificial wing and this model are adjusted to model both modes as they are in the biological wing, this model can inform aerodynamic studies on insect wings.

Future iterations of this wing model will be designed to accurately model the first and second mode. Once that design is obtained, these wings can be used in controlled wing studies for virtually unlimited time periods, which is not currently an option when using biological specimens due to the rate at which the wings desiccate once removed from the insect's body. Provided that the artificial wings dynamically behave like the biological wings during dynamic tests, this could revolutionize the way that insect wing experiments are carried out. Furthermore, the information in my research can inform future MAV wing designs, and potentially could be used as MAV wings and in other small-scale flexible airfoil applications.

REFERENCES CITED

[1] Helbling, E. Farrell, and Robert J. Wood. "A review of propulsion, power, and control architectures for insect-scale flapping-wing vehicles." Applied Mechanics Reviews 70.1 (2018): 010801

[2] Trimmer, William SN. "Microrobots and micromechanical systems." Sensors and actuators 19.3 (1989): 267-287

[3] Trimmer, William SN. "Microrobots and micromechanical systems." Sensors and actuators 19.3 (1989): 267-287

[4] Wood, Robert J., et al. "Progress on 'pico'air vehicles." The International Journal of Robotics Research 31.11 (2012): 1292-1302.

[5] Groen, Mark, et al. "Improving flight performance of the flapping wing MAV DelFly II." Int. Micro Air Vehicle Conf. and Competition (IMAV 2010) (Braunschweig, Germany). 2010.

[6] Ramezani, Alireza, et al. "Bat Bot (B2), a biologically inspired flying machine." 2016 IEEE International Conference on Robotics and Automation (ICRA). IEEE, 2016.

[7] Pornsin-Sirirak, T. Nick, et al. "Microbat: A palm-sized electrically powered ornithopter." Proceedings of NASA/JPL Workshop on Biomorphic Robotics. 2001.

[8] Wood, Robert J. "The first takeoff of a biologically inspired at-scale robotic insect." IEEE transactions on robotics 24.2 (2008): 341-347.

[9] Phan, Hoang Vu, and Hoon Cheol Park. "Remotely controlled flight of an insect-like tailless flapping-wing micro air vehicle." 2015 12th International Conference on Ubiquitous Robots and Ambient Intelligence (URAI). IEEE, 2015.

[10] Reid, Heidi E., et al. "Wing flexibility reduces the energetic requirements of insect flight." Bioinspiration & biomimetics 14.5 (2019): 056007.

[11] Norris, Aaron G. "Experimental Characterization of the Structural Dynamics and Aero-Structural Sensitivity of a Hawkmoth Wing Toward the Development of Design Rules for Flapping Wing Micro Air Vehicles." (2013).

[12] Dirks J-H, Taylor D. "Veins Improve Fracture Toughness of Insect Wings." PLoS ONE 7(8): e43411. https://doi.org/10.1371/journal.pone.004341. (2012)

[13] Watson, Gregory S., and Jolanta A. Watson. "Natural nano-structures on insects—possible functions of ordered arrays characterized by atomic force microscopy." Applied surface science 235.1-2 (2004): 139-144.

[14] Ko, Jin Hwan, et al. "Micro/nanofabrication for a realistic beetle wing with a superhydrophobic surface." Bioinspiration & biomimetics 7.1 (2012): 016011.

[15] Combes, S. A., and T. L. Daniel. "Flexural stiffness in insect wings I. Scaling and the influence of wing venation." Journal of experimental biology 206.17 (2003): 2979-2987.

[16] Combes, S. A., and T. L. Daniel. "Flexural stiffness in insect wings II. Spatial distribution and dynamic wing bending." Journal of Experimental Biology 206.17 (2003): 2989-2997.

[17] Sims, Travis W., Anthony N. Palazotto, and Aaron Norris. "A structural dynamic analysis of a *Manduca sexta* forewing." International Journal of Micro Air Vehicles 2.3 (2010): 119-140.

[18] Ma, Yun, et al. "Functional morphology and bending characteristics of the honeybee forewing." Journal of Bionic Engineering 14.1 (2017): 111-118.

[19] Song, F., K. L. Lee, A. K. Soh, F. Zhu, and Y. L. Bai. “Experimental studies of the material properties of the forewing of cicada”. The Journal of Experimental Biology, 207:3035–3042, 2004.

[20] Talucdher, R., and Kunigal S. "Tensile properties of veins of damselfly wing." Journal of Biomaterials and Nanobiotechnology 4.03 (2013): 247.

[21] Ennos, A. R. "The inertial cause of wing rotation in Diptera." Journal of experimental biology 140.1 (1988): 161-169.

[22] Sims, T. W., Palazotto, A. N., Norris, A. "A structural dynamic analysis of a *Manduca sexta* forewing." International Journal of Micro Air Vehicles 2.3 (2010): 119-140.

[23] Chen, Jen-San, Jeng-Yu Chen, and Yuan-Fang Chou. "On the natural frequencies and mode shapes of dragonfly wings." Journal of Sound and Vibration 313.3-5 (2008): 643-654

[24] San Ha, Ngoc, et al. "Relationship between wingbeat frequency and resonant frequency of the wing in insects." Bioinspiration & biomimetics 8.4 (2013): 046008

[25] DeLeón, N. E., and Palazotto, A. "The evaluation of a biologically inspired engineered MAV wing compared to the *Manduca sexta* wing under simulated flapping conditions." International Journal of Micro Air Vehicles 3.3 (2011): 149-168.

[26] Moses, K. C., et al. "Artificial Manduca sexta forewings for flapping-wing micro aerial vehicles: how wing structure affects performance." Bioinspiration & biomimetics 12.5 (2017): 055003.

[27] Liu, Zhiwei, et al. "Artificial insect wings with biomimetic wing morphology and mechanical properties." Bioinspiration & biomimetics 12.5 (2017): 056007.

[28] Ha, N. S., et al. "Static and dynamic characteristics of an artificial wing mimicking an Allomyrina dichotoma beetle's hind wing for flapping-wing micro air vehicles." Experimental mechanics 52.9 (2012): 1535-1549.

[29] Rajabi, H., M. Moghadami, and A. Darvizeh. "Investigation of microstructure, natural frequencies and vibration modes of dragonfly wing." Journal of Bionic Engineering 8.2 (2011): 165-173.

[30] Fitzgerald, Timothy. Nonlinear fluid-structure interactions in flapping wing systems. Diss. 2013.

[31] Willmott, A. P., and Ellington, C. P., "The Mechanics Of Flight In The Hawkmoth *Manduca Sexta*, I. Kinematics Of Hovering And Forward Flight", Journal of Experimental Biology, (1997), Vol. 200, No. 21, pp. 2705-2722.

[32] Dai, H., Haoxiang L., and Doyle, J. F. "Dynamic pitching of an elastic rectangular wing in hovering motion." Journal of Fluid Mechanics 693 (2012): 473-499.

[33] Jankauski, M., Guo, Z., and Shen, I. Y.. The effect of structural deformation on flapping wing energetics. Journal of Sound and Vibration, 429:176–192, (2018).

[34] MatWeb, LLC. Overview of materials for Brass. From http://www.matweb.com/search/datasheet_print.aspx?matguid=d3bd4617903543ada92f4c101c2a20e5. Accessed November 15, 2019.

[35] Smith, M. (2009). ABAQUS/Standard User's Manual, Version 6.9. Providence, RI: Dassault Systèmes Simulia Corp.

[36] Appl, F. C., and N. R. Byers. "Fundamental frequency of simply supported rectangular plates with linearly varying thickness." Journal of Applied Mechanics 32.1 (1965): 163-168.

[37] Blevins, R. D. "Natural frequencies of shallow cylindrically curved panels." Journal of Sound and Vibration 75.1 (1981): 145-149.

[38] Ennos, A. R. "Mechanical behaviour in torsion of insect wings, blades of grass and other cambered structures." Proceedings of the Royal Society of London. Series B: Biological Sciences 259.1354 (1995): 15-18.

[39] Willmott, Alexander P., and Charles P. Ellington. "The mechanics of flight in the hawkmoth *Manduca sexta*. II. Aerodynamic consequences of kinematic and morphological variation." Journal of Experimental Biology 200.21 (1997): 2723-2745.

[40] Bell, R. A., C. G. Rasul, and F. G. Joachim. "Photoperiodic induction of the pupal diapause in the tobacco hornworm, *Manduca sexta*." Journal of insect physiology 21.8 (1975): 1471-1480.

[41] Dynamic Design Solutions (DDS) NV. (2017) FEMtools Modal Parameter Extractor User's Guide, Version 4.0.1.

[42] Mathworks. (2019). Modalfit (R2019b). Retrieved November 12, 2019 from https://www.mathworks.com/help/signal/ref/modalfit.html#bvogfwe.

[43] Ennos, A. Roland. "The importance of torsion in the design of insect wings." Journal of experimental Biology 140.1 (1988): 137-160.

[44] MatWeb, LLC. Overview of materials for Low Density Polyethylene (LDPE). From http://www.matweb.com/search/DataSheet.aspx?MatGUID=9ff98d958a714b2a8a00990a929d6f14. Accessed November 14, 2019.

[45] MatWeb, LLC. Overview of materials for Polylactic Acid (PLA) Biopolymer. From http://www.matweb.com/search/DataSheet.aspx?MatGUID=ab96a4c0655c4018a8785ac4031b9278&ckck=1. Accessed November 14, 2019.

APPENDICES

APPENDIX A

MATLAB CODES

APPENDIX A.1: CURVE FITTING ALGORITHM USED TO DETERMINE NATURAL FREQUENCIES AND DAMPING RATIOS

```
%MJ%
clear all;close all;clc;
```

LOAD DATA

```
%Csvread('filename',# row where data starts, #column where data starts)
Dat=csvread('Data.csv',6,0);

%Index the data
F=Dat(100:700,1); %pulls the frequency column in Hz
Real=Dat(100:700,2); % pulls the real part of the FFT
Imag=Dat(100:700,3); % pulls the imagninary part of the FFT

FFT=Real+i*Imag; %This compiles the actual FFT data

%To make sure the FFT looks the same as it did in Polytec, we can plot it.
%We want to plot the magnitude here, which is sqrt(Real^2+Imag^2)

FFT_Mag=sqrt(Real.^2+Imag.^2);

figure()
plot(F,FFT_Mag)
title('FFT Magnitude')
xlabel('f (Hz)')
ylabel('m/s / (m/s^2)')
```

CURVE FITTING

```
%Now we can do the curve fitting using the modal fit function.  The syntax
%is as follows:

% modalfit(FFT of data , frequency vector ,sampling frequency ,% of modes you want to
extract,'FitMethod',whatever algorithm you want to use)

% there are three built in algorithms:

%'lsce' – Least-Squares Complex Exponential Method. If you specify 'lsce', then fn is a
vector with mnum elements, independent of the size of frf.
%'lsrf' – Least-squares rational function estimation method. If you specify 'lsrf', then
fn is a vector with mnum elements, independent of the size of frf. The method is
described in [3]. See Continuous-Time Transfer Function Estimation Using Continuous-Time
```

```
Frequency-Domain Data (System Identification Toolbox) for more information. This
algorithm typically requires less data than nonparametric approaches and is the only one
that works for nonuniform f.
%'pp' – Peak-Picking Method. For an frf computed from n excitation signals and m response
signals, fn is an mnum-by-m-by-n array with one estimate of fn and one estimate of dr per
frf.


% the outputs of the modalfit are:

%fn - estimated natural frequency(or multiple)
%dr - damping ratio
%ms - mode shape
%ofrf - fitted FRF

% we can compare each to see how they line up with the raw data

[fn_pp,dr_pp,ms_pp,ofrf_pp] = modalfit(FFT,F,2560,2,'FitMethod','PP');
[fn_lsrf,dr_lsrf,ms_lsrf,ofrf_lsrf] = modalfit(FFT,F,2560,2,'FitMethod','lsrf');
[fn_lsce,dr_lsce]= modalfit(FFT,F,2560,2);

disp('estimated natural frequencies by three algorithms')
fn_pp
dr_pp
fn_lsrf
dr_lsrf
fn_lsce
dr_lsce
% note that abs(FFT) = sqrt(Real.^2+Imag.^2) ; at least with how MATLAB
% computes it

figure()
plot(F,abs(FFT),F,abs(ofrf_pp),'--',F,abs(ofrf_lsrf),'--')
title('FFT Magnitude')
xlabel('f (Hz)')
ylabel('m/s / (m/s^2)')
legend('Raw','PP','LSRF')
xlim([0 250])
```

FILTER DATA

```
%There are problems with both.  We may need to filter the data beforehand
%to remove some noise:

%We apply a moving average filter, which averages data points +/- 'k'
%values (here, I've used two -- the fewer the better, otherwise we start
%to distort the signal)
```

```
FFT_Filt=movmean(Real+i*Imag,2);

figure()
plot(F,abs(FFT),F,abs(FFT_Filt))

[fn_pp,dr_pp,ms_pp,ofrf_pp] = modalfit(FFT_Filt,F,2560,2,'FitMethod','PP');
[fn_lsrf,dr_lsrf,ms_lsrf,ofrf_lsrf] = modalfit(FFT,F,2560,2,'FitMethod','lsrf');


disp('estimated natural frequencies by three algorithms (after applying moving mean to
pre-filter data)')
fn_pp
dr_pp
fn_lsrf
dr_lsrf
fn_lsce
dr_lsce


figure()
plot(F,abs(FFT),F,abs(ofrf_pp),'--')
title('FFT Magnitude')
xlabel('f (Hz)')
ylabel('m/s / (m/s^2)')
legend('Raw','PP')
xlim([0 150])
```

Published with MATLAB® R2018b

APPENDIX A.2: CURVATURE POINT FIELD MAPPING MATLAB CODE

```
%MJ%
close all;clear all;clc;
```

SELECT THESE VARIABLES

```
X_Shift=18.5;
Y_Shift=-25.086+2.85;
Z_Shift=40;
ROTATE=10;
```

```
%Load all data for surface curve, membrane nodes and vein nodes
Curve_Dat=load('curved surface v1.txt');
Membrane_Dat=load('Membrane.txt');
Venation_Dat=load('Venation.txt');

OG_Memb=Membrane_Dat;
OG_Ven=Venation_Dat;

%The curve is in units 'm', so we need to convert to 'mm'
Curve_Dat=Curve_Dat*1000;

%Moreover, it looks like the 'z' axis is backwards in the curvature file,
%so we will multiply it by -1 to reverse it
XCurve=-Curve_Dat(:,1);
YCurve=Curve_Dat(:,2);
ZCurve=-1*Curve_Dat(:,3);


figure()
plot3(XCurve,YCurve,ZCurve,'r*'); hold on;
plot3(Membrane_Dat(:,2),Membrane_Dat(:,3),Membrane_Dat(:,4),'g*')
grid on
xlabel('x')
ylabel('y')
zlabel('z')
title('Membrane superimposed on surface mold')
```

```
X_OG=9;
XCurve=XCurve+X_OG

figure()
plot3(XCurve,YCurve,ZCurve,'r*'); hold on;
plot3(Membrane_Dat(:,2),Membrane_Dat(:,3),Membrane_Dat(:,4),'g*')
```

```
grid on
xlabel('x')
ylabel('y')
zlabel('z')
title('Membrane superimposed on surface mold')



for i=1:length(XCurve)
    Ry=[cosd(ROTATE) 0 -sind(ROTATE);0 1 0;sind(ROTATE) 0 cosd(ROTATE)];
   XCurve(i)=dot(Ry*[XCurve(i);YCurve(i);ZCurve(i)],[1;0;0]);
   YCurve(i)=dot(Ry*[XCurve(i);YCurve(i);ZCurve(i)],[0;1;0]);
   ZCurve(i)=dot(Ry*[XCurve(i);YCurve(i);ZCurve(i)],[0;0;1]);

end

scalar=0.7;


XCurve=XCurve+X_Shift;
YCurve=scalar*YCurve+Y_Shift;
ZCurve=ZCurve+Z_Shift;

figure()
plot3(XCurve,YCurve,ZCurve,'r*'); hold on;
plot3(Membrane_Dat(:,2),Membrane_Dat(:,3),Membrane_Dat(:,4),'g*')
grid on
xlabel('x')
ylabel('y')
zlabel('z')
title('Membrane superimposed on surface mold')
view([0 0])


fitobject = fit([XCurve,ZCurve],scalar*YCurve,'poly33');

for i=1:length(Membrane_Dat(:,2))
Membrane_Dat(i,3)=feval(fitobject,[Membrane_Dat(i,2) Membrane_Dat(i,4)]);
end

for i=1:length(Venation_Dat(:,2))
Venation_Dat(i,3)=feval(fitobject,[Venation_Dat(i,2) Venation_Dat(i,4)]);

end

figure()
plot3(XCurve,YCurve,ZCurve,'r*'); hold on;
plot3(Venation_Dat(:,2),Venation_Dat(:,3),Venation_Dat(:,4),'bo')
plot3(Membrane_Dat(:,2),Membrane_Dat(:,3),Membrane_Dat(:,4),'gx')

grid on
```

```
xlabel('x')
ylabel('y')
zlabel('z')
title('Membrane superimposed on surface mold')
view([0 0])
```

Published with MATLAB® R2018b

APPENDIX B

DIRECTIONALLY 3D PRINTED BEAM MODAL ANALYSIS

Two sets of 3D printed ABS beams (dimensions 12.5 cm x 1.5 cm x 1 cm) were subject to the same modal tests as the wings to determine how print orientation may affect stiffness in the wings. Two different directions were tested: (1) printed vertically and at a 0° offset; (2) printed vertically and at 90° offset. The set of beams printed vertically and at a 0° offset show an average first natural frequency of 95.84 Hz, and the set printed vertically and at 90° offset show an average first natural frequency of 148.48 Hz (full data set shown in Table B.1). This data shows that 90° directional change can lead to a 150 percent increase in first natural frequency for ABS. It suggests that there may be the potential for this directional change to cause an increase in natural frequency of printed PLA, as well, but more directional data will need to be gathered, and PLA should be used for a full understanding of how print orientation may affect our artificial wings. This data is preliminary and warrants further investigation in future work if directional printing is used in future wing iterations.

Table B.1 First natural frequencies and the associated averages and standard deviations for the directionally printed beams.

Sample	**ω_1 (Hz)**	**Average**	**St. Dev.**
0, vertical 1	100.789		
0, vertical 2	97.378	99.0835	1.7055
0, vertical 3	95.902		
0, vertical 4	97.719		
0, vertical 5	93.376	95.66567	1.78088
0, vertical 6	95.287		
0, vertical 7	97.781		
0, vertical 8	94.975	96.01433	1.255699
90, vertical 1	149.827		
90, vertical 2	154.125		
90, vertical 3	148.349	150.767	2.449931
90, vertical 4	145.83		
90, vertical 5	150.729		
90, vertical 6	147.349	147.9693	2.047545
90, vertical 7	143.248		
90, vertical 8	146.558		
90, vertical 9	144.059	144.6217	1.408657
90, vertical 10	158.087		
90, vertical 11	145.908		
90, vertical 12	147.706	150.567	5.367867

APPENDIX C

BIOLOGICAL WING MASS DISTRIBUTION CUT PATTERN

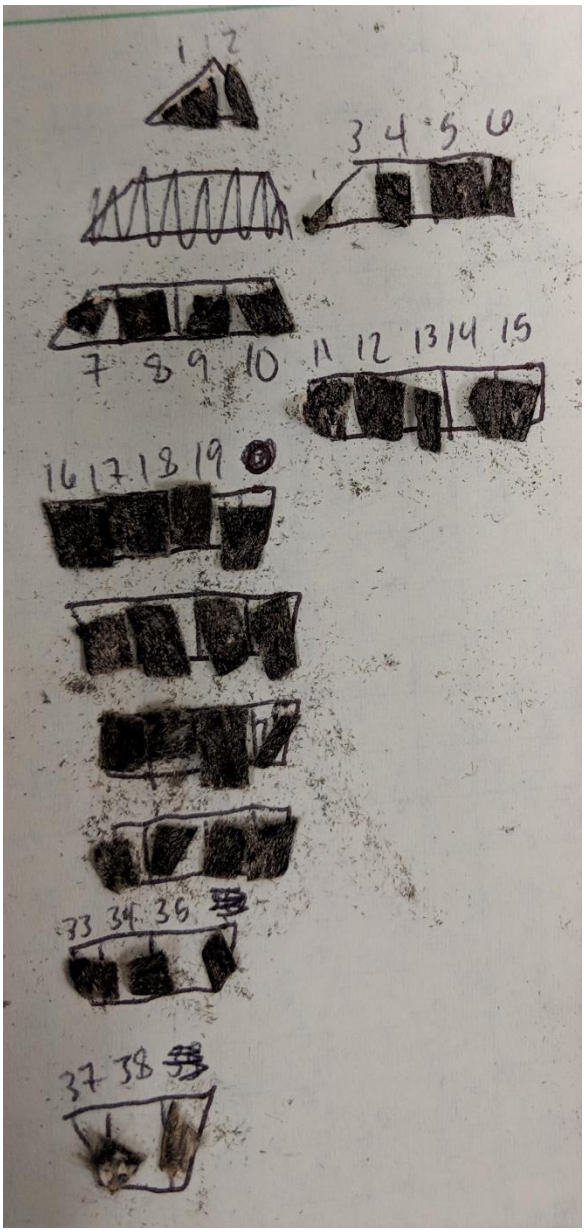

Figure C.1: Thirty-six sections of the hawkmoth wing were produced during the cut-and-weigh experiment to determine mass distributions. Each are approximately 5 mm x 5 mm. The wing is mapped into the sections shown above to keep track of where each section belonged. The sections are separated to prevent static cling between pieces.